Title

Decoupling Retinal Input from its Physiological Constraints

ISBN

9798189279805

Author

Doyle, Hannah Kay

Publication Date

2026-05-01

Peer reviewed|Thesis/dissertation

Decoupling Retinal Input from its Physiological Constraints

by

Hannah Kay Doyle

A dissertation submitted in partial satisfaction of the

requirements for the degree of

Doctor of Philosophy

in

Electrical Engineering and Computer Science

in the

Graduate Division

of the

University of California, Berkeley

Committee in charge:

Professor Ren Ng, Chair
Professor Austin Roorda
Professor William S. Tuten
Professor Boubacar Kanté

Spring 2026

Decoupling Retinal Input from its Physiological Constraints

Abstract

Decoupling Retinal Input from its Physiological Constraints

by

Hannah Kay Doyle

Doctor of Philosophy in Electrical Engineering and Computer Science

University of California, Berkeley

Professor Ren Ng, Chair

The human visual system is constrained by its physiological implementation. The imperfect optics of the cornea and lens blur the light arriving at the retina. The inherent spectral sensitivity functions of the retina's three cone photoreceptor types give rise to the allowable gamut of colors that humans can perceive. The mosaic-like tiling arrangement of those cone cells in the retina dictates the spatial sampling characteristics of the eye, limiting the resolution with which one can perceive fine spatial detail. Even under fixation, the eye's constant motion causes the retinal image to shift continuously across the photoreceptor mosaic. Together, these consequences of human biology impose constraints on visual perception under natural viewing conditions. However, through recent advances in retinal imaging and stimulation technology, we bypass these constraints through unnaturally precise spatial control of light at the retinal interface, allowing for manipulation of the inputs to the visual system at the level of individual photoreceptors. By gaining control of cone activations at the cellular scale, we push past the spectral and spatial boundaries of the human visual system.

This work explores color and spatial vision beyond the physiological restrictions of typical viewing conditions. Chapter 1 provides background on those restrictions and the optical instrument used to make such experiments possible through simultaneous imaging, eye-tracking, and stimulation. Each subsequent chapter outlines the application of this technology to perform psychophysical experiments which probe the human color and spatial vision system outside of its typical operating conditions. Chapter 2 studies color perception of wavelengths outside the visible spectrum by eliciting 2-photon absorption of infrared light in photoreceptor cells. Chapter 3 shows humans a color with a saturation beyond the boundary of the human color gamut using targeted stimulation of individual cone photoreceptors. Chapter 4 tests the spatial limits to vision, imposing emulated photoreceptor loss on the retina and finding where visual acuity breaks down as a result. These experiments offer insight into the way color and spatial vision arise from the signals delivered to the retina, by enacting control over the input while simultaneously measuring the resulting sensory output.

Contents

List of Figures

Acknowledgments

I would like to thank Ren Ng, whose enthusiasm was the reason that I chose to come to Berkeley for graduate school. He encouraged me to be ambitious and taught me a great deal about conducting research and communicating scientific results. I would like to thank Austin Roorda, who always made time to serve as the subject in my hours-long experiments despite his busy schedule. I feel very lucky to have had him as the mentor who brought me into the field of vision science. I want to thank all of my labmates from the Ng, Roorda, and Tuten labs who provided community through many trips out for coffee and lunches on Minor Beach.

I am very grateful to my family, who would support me in any path I decided to pursue, and make me feel so loved every day. I want to thank James Fong, who I was fortunate to work closely with for years on the Oz Vision project. James is brilliant but never arrogant, and was always happy to help when I came to him. I would like to thank Josephine D'Angelo, who has become my best friend through this experience, and who walked home from work with me every day even though she could have biked. When I think back to graduate school, working alongside her will be the part that I miss most. Finally, I would like to thank my partner Jacob, whose love and support got me through every day.

Chapter 1

Introduction

The study of human vision using conventional methods is obscured by physiological factors that enact layers of transformation between the light entering the eye and the signals generated at the retinal interface. Here, we employ advances in high-precision optical stimulation to modulate retinal input more directly than previously possible. In doing so, we bypass the spectral, chromatic, and spatial constraints imposed by human physiology. In Chapter 2, we study human perception of wavelengths that fall beyond the visible range and show that tight focusing of light at the cones imparts a 25-fold boost in its visibility. In Chapter 3, we show humans a color "olo" whose saturation lies outside of the gamut of human color vision that is achievable under ordinary viewing. Finally, in Chapter 4, we isolate the role of the retinal mosaic in mediating spatial vision and show that eye motion provides a compensatory benefit for acuity under cone cell loss. These experiments taken together characterize human visual perception outside of its spectral, chromatic, and spatial limits.

1.1 Physiological Limits to Vision

At the back of the eye sits the retina, the light-sensitive tissue which acts as the interface converting light from the external world into sensory signals reaching the brain. This conversion takes place in photoreceptor cells that tile the retinal mosaic. These cells themselves belong to distinct spectral classes which dictate their relative sensitivity to light across the visible spectrum under daytime conditions. Together, these physiological features of the retina impose constraints on the input to the human visual system.

There are additional layers of processing which follow the initial activation of the photoreceptors that shape the visual percept. Signals generated by the cones feed into retinal ganglion cells, which often pool responses from several cones [1]. Ultimately, the outputs from roughly 5 million cone cells in total are reduced to roughly 1 million optic nerve fibers exiting the eye, resulting in significant compression on the signals produced at the retinal interface [2, 3]. Beyond the retina, sensory signals face multiple stages of higher-level visual processing in the brain [4, 5]. In this work, we focus on manipulating the retinal input, and

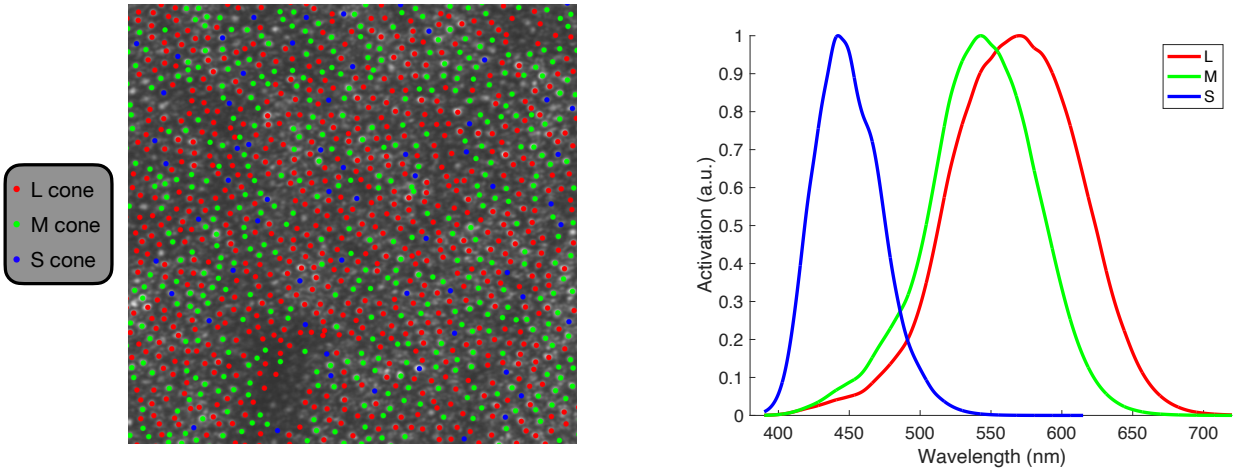

Figure 1.1: **Cone spectral types and their spectral sensitivity functions.** A retinal image from 4° eccentricity is shown on the left with labels indicating the L (red), M (green), and S (blue) cones. The spectral sensitivity for each cone type (a.u.) is plotted as a function of wavelength on the right. L, M, and S cones are primarily sensitive to long, medium, and short wavelengths, respectively.

therefore will primarily consider the factors that directly shape it, namely the eye's optics and the characteristics of the retinal mosaic.

Factors constraining human color vision

The retina contains photoreceptor cells that absorb light, providing the inputs to the visual system that lead to perception. These cells belong to two broad categories, known as rods and cones, which operate at different light levels in order to establish the retina's wide dynamic range. Rods are primarily active at dim scotopic light conditions while cones dominate at brighter photopic light levels, and both cell types contribute in the mesopic range between the two [6]. While rods mediate night vision, cones facilitate daytime vision and inform the visual system about color.

Photoreceptor cells detect light through absorption of photons by photopigments. Photopigments themselves consist of opsin, a protein, which is bound to the 11-*cis*-retinal chromophore, a light-sensitive molecule. When a photon is absorbed by the chromophore, it undergoes a conformational change, which in turn causes the opsin to change shape and become active. These two conformational changes trigger a cascade that ultimately results in a change in the photoreceptor cell membrane potential which transmits an electrical signal to downstream retinal neurons [7].

In the typical human retina, there are three types of cone cells, distinguished by their

spectral sensitivity functions. These types are designated L, M, and S cones, indicating their sensitivity to long, medium, and short wavelengths, respectively [8, 9]. A retinal mosaic labeled with the three types along with their sensitivity functions is shown in Figure 1.1. The sensitivity functions dictate the degree to which each cone type is activated in response to varying wavelengths of light, and are a direct result of their genetic makeup. Genes encode different opsins for the L, M, and S cones which dictate the spectral tuning of the chromophore that they bind to [10]. Then, the combined activation levels of the three cone types serve as a basis for encoding color information.

The consequences of the trichromatic cone mosaic for color vision are twofold. First, one can see that the spectral sensitivities span a finite range of wavelengths. That is, there is an upper and lower wavelength bound outside of which the L and S cones no longer respond. This defines the visible spectrum of wavelengths, ranging from approximately 400-700 nm. Wavelengths outside of this range are typically not perceptible under standard viewing conditions.

Second, the shapes and relative positioning of the L, M, and S spectral sensitivity functions form the space of colors that humans can see. One can visualize this by constructing a chromaticity diagram that shows the gamut of human color vision, representing all possible combinations of cone activation levels [11]. Figure 1.2 shows the LMS triangle chromaticity diagram, a ternary plot where the three vertices correspond to pure L, M, and S activation respectively. To establish the bounds of the human color gamut, one can sweep across all wavelengths in the visible spectrum and plot the relative LMS activations at each wavelength on the triangle. This is known as the spectral locus, the edge of the human color gamut that is derived directly from the spectral sensitivities themselves. Under normal viewing conditions, this edge corresponds to the most saturated colors that humans can perceive.

Points along the spectral locus correspond to monochromatic light, whereas mixtures of pure light will lie on a line connecting their spectral components. One such line is the line of purples, which represents mixtures of long- and short-wavelength light and acts as a non-spectral closure connecting the endpoints of the spectral locus. Then, any spectrum of light is a weighted combination of pure wavelengths and thus lies at a point within the convex hull defined by the spectral locus and line of purples. That is, the gamut of human color vision can be represented as the area bounded by the spectral locus and line of purples, which is shown as the rainbow region in Figure 1.2 [12].

Notably, the rainbow region representing the gamut of human color vision does not cover the entire area of the LMS triangle. This is due to a feature of the LMS sensitivities themselves, namely that the M cone spectral sensitivity overlaps completely with the L and S sensitivity functions. As a result, any light that activates M cones will also activate L cones, S cones, or both. Thus, there are certain combinations of L, M, and S activations that are forbidden by this feature of the LMS sensitivities. These are the points which lie outside of the human color gamut, represented by the empty area in Figure 1.2. There is no spectrum of light that corresponds to these points.

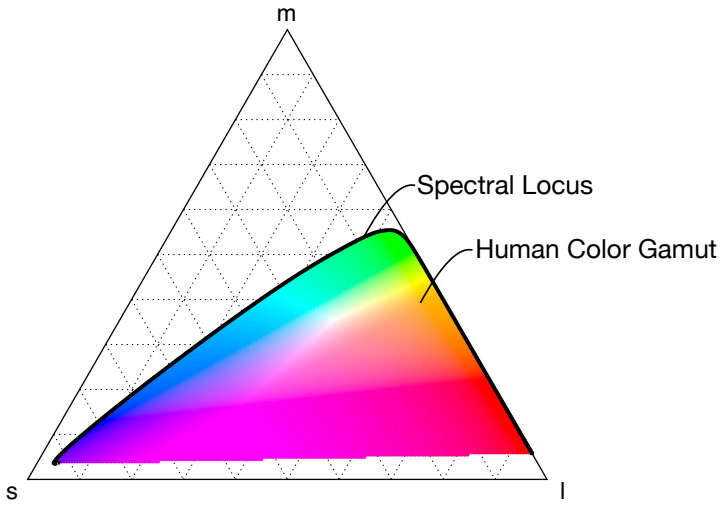

Figure 1.2: **LMS chromaticity triangle.** The ternary diagram visualizes color space with respect to the relative activation levels of the L, M, and S cones. The spectral locus is the result of plotting these activation levels for monochromatic wavelengths spanning the visible spectrum. The human color gamut is the convex hull bounded by the spectral locus, colored to approximate the appearance corresponding to each point in color space. The white region outside of the human color gamut represents the patterns of L, M, and S, activation that are impossible to achieve under natural viewing due to overlap in the spectral sensitivities.

Factors constraining human spatial vision

Light from the external world undergoes several modifications in the process of being converted to sensory signals reaching the brain. First, the aberrations of the eye impart blur as light travels through the eye's optics. Second, the eye is constantly in motion, even when one fixates on a target. Thus, the blurred light landing on the retina is also translated across it due to the eye's motion. Finally, the light is sampled by the discrete array of cone photoreceptor cells that tile the retina. In combination with postreceptoral stages of processing, these layers of transformation jointly determine the finest level of spatial detail that can be resolved by the human visual system.

The optics of the eye are imperfect due to the non-ideal shape of the cornea and lens [13, 14]. These aberrations can be broken down into their constituent components and represented by Zernike polynomials [15]. Lower order aberrations such as defocus and astigmatism dominate in day-to-day vision and can be corrected with prescription lenses. However, higher order Zernike modes such as coma, trefoil, and spherical aberration remain uncorrected. These become especially significant as pupil size increases [16], which is the case in

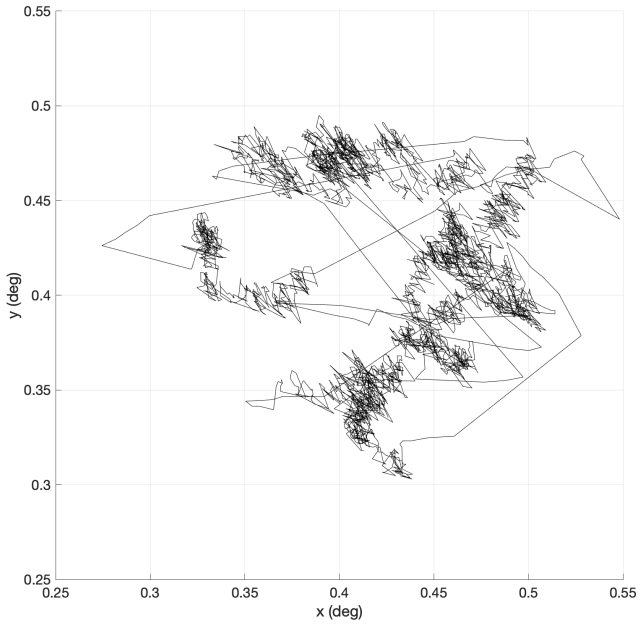

Figure 1.3: **Sample eye motion trace.** A real recorded eye motion trace is plotted showing the x- and y- position of the eye in degrees during a period of fixational eye motion. Segments of drift appear jagged on the plot and are periodically interrupted by microsaccades, which correspond to straight line segments where the eye moves a greater distance.

many vision experiments which require dilation. The size of the blur resulting from these aberrations spans several cones at the fovea, thus complicating precise stimulation of those cells.

In addition to monochromatic aberrations, the eye's optics also introduce wavelength-dependent chromatic aberrations [17]. This includes longitudinal chromatic aberration, where wavelengths are focused at different depths in the eye, spanning approximately 2 D across the visual range [18], as well as transverse chromatic aberration, where wavelengths land at different locations on the retina [19, 20]. While typically not noticeable in everyday vision, these sources of error become relevant when studying vision at the cell level with multi-wavelength displays, as the differences in light delivery between wavelengths can span several cone cells.

In addition to the spatial blurring of light incident on the retina, visual stimuli are temporally spread across the retina due to the eye's constant motion. Even while trying to fixate on a visual target, the eye exhibits fixational eye motion with periods of drift and microsaccades as shown in Figure 1.3. This motion varies in magnitude between individuals, with average drift velocities typically on the order of 50 arcmin/s [21]. This is significant in

scale compared to the size of a cone cell, which ranges from 0.5 - 2 arcmin [22, 2]. It has been shown that the presence of eye motion has an effect on visual acuity and spatial vision [23, 24, 25, 26].

After being altered by the eye's optics and motion, the retinal image is discretized into individual activation levels by the cone photoreceptors, which tile the retina in a mosaic-like arrangement [27]. The density of this array of cells varies across the retina. At the center of the retina in the fovea, the average reported spatial density is 199,000 cones/mm^2, with densities ranging from 100,000 - 324,000 cones/mm^2 between people [2]. Further from the fovea, cone density decreases sharply with increasing eccentricity. This sets a baseline sampling limit for resolving fine visual detail [28]. However, the impact of the retinal mosaic on the sampling limits of the visual system is entangled with the effects of the eye's imperfect optics and motion.

1.2 Cone-Targeted Stimulation

Study of the human visual system is clouded by the physiological constraints described above. Under traditional display methods, the input signal to the visual system is the result of light coming from that display being modified by the aberrations of the eye, translated on the retina due to the eye's motion, and sampled by the retina's discrete array of cone photoreceptors and their various spectral types. Thus, these factors cannot be decoupled and studied independently under conventional methods.

The work described in subsequent chapters utilizes the most recent advances in retinal stimulation in order to bypass the constraints imposed by the optical aberrations of the eye, eye motion, and the spectral and spatial characteristics of the retinal mosaic. A sequence of technological breakthroughs were necessary in order to make this possible. First, adaptive optics was used to correct for the eye's aberration in order to produce images of the retinal mosaic. The sharp focusing ability that comes from an adaptive optics correction then enabled the delivery of visible stimuli comparable to the size of individual cones. Next, the complications introduced by eye motion were compensated for with the introduction of retinal-image based eye tracking and retinally-stabilized stimuli. This enabled the targeting of individual cone cells, which was then scaled up with hardware and software improvements to population scales of cones. Finally, with additional methods for characterizing the spectral types of cones in the retinal mosaic, these advancements culminated in Oz, a principle for creating visual percepts cone-by-cone, enabling unprecedented control over the input to the human visual system.

Adaptive optics scanning light ophthalmoscopy

Optical quality in the human eye is limited by aberrations in the cornea and lens, which in turn impede our ability to image the smallest features on the retina [13]. Through Adaptive Optics Scanning Light Ophthalmoscopy (AOSLO), we can use a closed-loop correction of

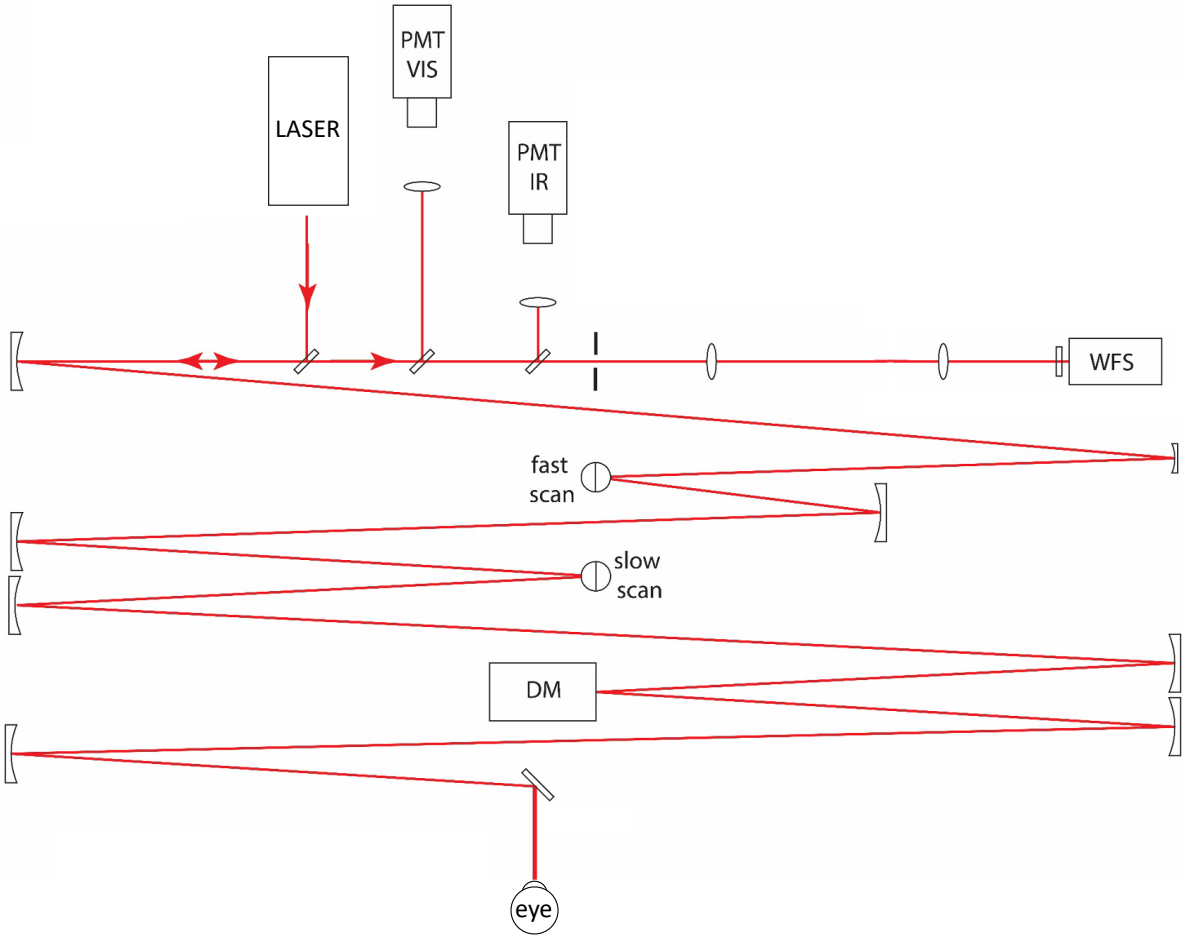

Figure 1.4: **AOSLO schematic diagram (courtesy Austin Roorda).** A simplified visualization of the Adaptive Optics Scanning Light Ophthalmoscope shows its main components. The light source is a laser, whose output is routed through the system by a series of concave mirrors to the eye. Along its path, it is scanned in a raster pattern by a slow vertical and fast horizontal scanner. The incident light is reflected from the retina and travels back through the system where it is split into wavelength channels by dichroic mirrors and measured by photomultiplier tubes (PMTs) and a wavefront sensor (WFS). The wavefront sensor measures the shape of the returning wavefront, which then informs the shape of the deformable mirror (DM). These two components operated in a closed feedback loop to flatten the wavefront and produce a sharply focused spot of light at the retina.

those aberrations to both image the back of the eye with sufficient precision to see individual cells, and to deliver sharp focused spots of light at cellular scale [29, 30]. When done simultaneously, these capabilities enable psychophysical experiments that offer insight into the way perception arises from discrete cone photoreceptor signals.

A representative schematic diagram of an AOSLO is shown in Figure 1.4. This highlights the main components, which vary between specific system implementations. The light source is often a laser, whose output is relayed by a series of curved mirrors through the system to reach the eye. This light is reflected off of the back of the eye and travels back through the optical setup to be detected by the imaging and wavefront sensing arms.

A critical component of this system is the adaptive optics correction. The adaptive optics component is made up of a wavefront sensor (WFS) and deformable mirror (DM), which operate in a closed loop to correct for the eye's optical aberrations. Using the measurement of the eye's wavefront from the wavefront sensor, an array of actuators in the deformable mirror react accordingly to shape the mirror and flatten the wavefront at the pupil plane. The changes made on the deformable mirror in turn change the measurement made at the wavefront sensor, creating a feedback loop that works continuously to maintain a stable correction. Under the laws of diffraction, a larger pupil size produces a smaller focused spot at the retina. However, as pupil size increases, the higher-order aberrations of the eye also become more prominent [31, 16]. Adaptive optics compensates for these aberrations, allowing for the use of a dilated pupil while exploiting the benefits for tight focusing at the retina.

Thus far, these system components are sufficient to produce a focused spot of light at the retina; however, the desired outcome is to produce images of the retina and stimulate it over an extended region. Thus, the system contains two scanners in the optical path that move orthogonally in two dimensions. Together, they move the focused spot of light in a raster pattern on the retina in order to image and stimulate over that region.

The light reflected from the retina travels back through the system and thus is de-scanned upon its double-pass through the scanning elements. A sequence of filters split the returning light by wavelength channel such that each channel's light is delivered to the to the corresponding imaging or wavefront sensing arm. The imaging arms consist of detectors, often with confocal pinholes positioned in front of them to reject out-of-focus light and improve contrast of the retinal image. The benefit in image quality provided by adaptive optics is shown in Figure 1.5.

Cone-size stimuli

By correcting for the aberrations of the eye, adaptive optics allows for focusing of light more sharply at the retina than is possible under ordinary viewing. This enables the delivery of stimuli that are small enough to only activate single cones, offering a way to probe visual function at the cellular level. Prior work delivered 0.33-arcmin unstabilized flashes of visible light to the retina and asked subjects to report whether they saw the flashes and to name their hue [32]. Aside from one subject who tended to report a sensation of red, subjects

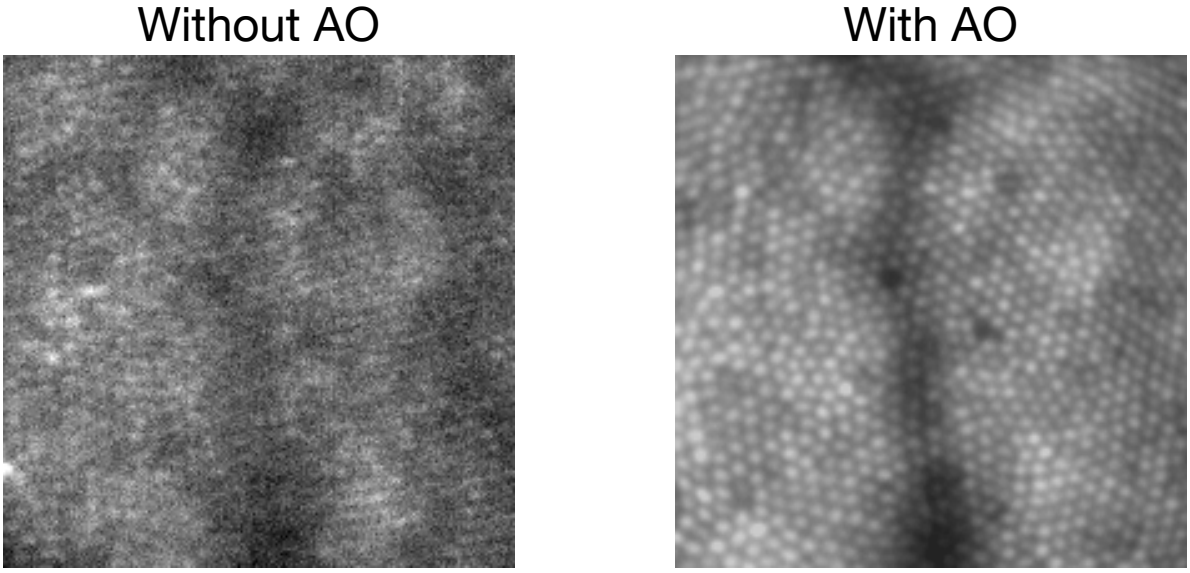

Figure 1.5: **Retinal imaging with and without adaptive optics (courtesy Austin Roorda).** A comparison is shown between two images taken at the same retinal location without (left) and with (right) an adaptive optics correction. Adaptive optics enables high-resolution imaging of the cone photoreceptor mosaic by compensating for the eye's imperfect optics.

responded with a wide range of color responses including white. This was in contrast to prior work that had only recorded red or green hue sensations when presenting small flashes of light intended to only activate L or M cones [33]. However, the flashes in these studies were delivered without the ability to stabilize them to the retina and without knowledge of the specific cones that they stimulated. Thus, it was not yet possible to correlate any given psychophysical response with any particular cone, leaving an opportunity for further advancement.

Retinally-stabilized stimulation

Even while fixating, the eye moves on a scale that is significant when compared to the size of a single cone cell. In order to send light to specific targets on the retina, it is therefore necessary to track the eye as it moves and use this tracking information to update the stimulation pattern with low latency. Prior work achieved offline tracking using a cross-correlation method to track a video of the moving retina against a single reference image [34]. Online tracking was then accomplished using a map-seeking circuit algorithm to track the live view of the retina and render stimuli that were fixed to target locations on the retina

[35]. Later work custom-designed a field-programmable gate array (FPGA) to reduce latency between the tracking and high-speed modulation of the laser's output such that stabilization error was reduced to 0.15 arcmin [36].

Cone-targeted stimulation

Later work combined the capabilities of cone-sized stimulation and retinal stabilization in order to perform targeted stimulation of individual cone cells. As an initial validation, small-spot detection experiments were conducted with this new technology [37]. Whereas prior work lacked certainty about which cones were being targeted, this work showed that it was possible to reliably target specific chosen cones by comparing detection thresholds between 543-nm flashes targeted at cones and at gaps between cones. Subjects reliably showed higher thresholds for detection in the gap-targeted case than the cone-targeted case. This demonstrated that the light delivery was precise enough to influence the activation levels of individual cones.

Cone cells belong to three different classes, each with different spectral sensitivity functions, but they cannot be distinguished by pure inspection of the retinal image. However, methods were developed in order to classify cones by their spectral type through densitometry [38] and later through optoretinography [39, 40, 41, 42]. Armed with cone classification information, new experiments were made possible that could connect color perception to specific cone cells of known type. Several experiments probed this by targeting individual cones in a classified retina with 543-nm light and asking subjects to report the resulting color experience [43, 44, 45]. Again, they found a large proportion of cones signaled white, irrespective of their type. When cones did signal a color, however, long-wavelength sensitive cones tended to signal red while medium-wavelength tended to signal green, despite the underlying light being the same in both cases. This demonstrated a connection between cone spectral type and color experience at the single-cone level.

Further work improved from one cone to two cones at a time in order to investigate how cone signals are combined to form color percepts [46]. This work revealed that saturation ratings were higher than expected by linear summation when two cones of the same spectral type were activated, and lower for two cones of different types. This work therefore began to show how an overall color experience arises through comparison between cone signals, in a way that is impacted by the spectral identities of those cones.

1.3 Summary of Contributions

The technical foundation described above presents an opportunity to manipulate the retinal input with high precision and probe the impact on visual perception. The work described in this dissertation exploits that opportunity by building on that technical foundation to achieve population-scale cone-by-cone stimulation and applying it to bypass spectral, chromatic, and spatial constraints on human vision.

Population-scale cone-by-cone stimulation

While measuring the color responses of individual cones provided some insight into the cellular basis for color vision, a gap remained between this highly specialized viewing condition and normal color vision, which derives inputs from many thousands of cones. In order to extend this capability to study color vision more broadly, we scale up these experiments accordingly.

In order to reliably perform stimulation over the entire AOSLO field of view, we track the eye's motion using a map of the retina that extends beyond that region. We create these retina maps using R-SLAM [47], a method developed by Jay Shenoy and James Fong. This method jointly solves for an underlying retinal image and an eye motion trace given a video of the moving retina. We therefore can give R-SLAM a series of videos spanning a large area in order to construct a map of the retina over that region, which is used for subsequent live tracking.

While prior work delivered very brief flashes of light to the retina, more sustained presentations would be necessary to more faithfully mimic normal viewing. This in turn requires reliably low latencies between tracking and stimulus updates. We use new software called Wizard, written by James Fong, which splits the incoming retinal image into strips for tracking and keeps latency between tracking and stimulus updates below 4 ms.

With sufficiently low latency and high bandwidth, Wizard enables programmable control over the stimulation of thousands of cones at a rate of 10^5 microdoses of light per second. This is the basis for the Oz principle of displaying color imagery [48]. Using the ability to target cones with laser light at population scales, we can in principle recreate arbitrary visual percepts by controlling the activation of each cone across the field of view. In this way, we gain access to the retinal input directly, allowing for psychophysical experiments that decouple this input from the physiological factors that typically constrain it.

Bypassing spectral, chromatic, and spatial constraints

The spectral sensitivity functions of the cones establish an approximate range of wavelengths that humans can perceive. However, one can perceive infrared wavelengths of light that fall beyond the visible range through 2-photon absorption in the cone photoreceptors if the spatiotemporal concentration of that light is sufficiently high [49]. In Chapter 2, we utilize the adaptive optics component of our system to elicit this effect through tight focusing of infrared light at the retina, imparting a 25-fold boost in the perceived luminance of infrared light as compared to the non-focused condition. Through color matching experiments, we characterize visual perception beyond conventional spectral limits.

In addition to determining the visible range of wavelengths, the cone sensitivities give rise to the shape of the human color gamut. In particular, the overlap in these sensitivities results in a forbidden region of theoretical LMS color space, corresponding to LMS activation levels that cannot be produced by any spectrum of light. In Chapter 3, we use the Oz principle to bypass those chromatic constraints on human color vision. We leverage precise, cone-

targeted laser stimulation to achieve these forbidden activations by targeting only the M cone cells. Through sustained presentation of these stimuli, we are able to characterize the resulting percept in color matching experiments. We show human subjects the color "olo," which appears as a blue-green hue with a saturation that lies beyond the spectral locus of the human color gamut.

Finally, we adapt the Oz system to explore the consequences of the retinal mosaic on spatial vision in Chapter 4. We eliminate the confound introduced by the eye's aberrations using adaptive optics to correct for them. We additionally account for the impact of eye motion by constructing two stimuli conditions that respond differently to fixational eye movements. Further, we implement programmable control over the effective sampling density of the retina by selectively stimulating varying proportions of cone cells. In this way, we are able to reveal the direct impact of decreasing sampling power on visual acuity, and show that eye motion provides a compensatory benefit under degradation of the retinal mosaic.

Chapter 2

Boosting 2-Photon Vision with Adaptive Optics

The 2-photon effect in vision occurs when two photons of the same wavelength are absorbed by a cone photopigment in the retina and create a visual sensation matching the appearance of light close to half their wavelength. This effect is especially salient for infrared light, where humans are mostly insensitive to 1-photon isomerizations and thus any perception is dominated by 2-photon isomerizations. This phenomenon can be made more readily visible using short-pulsed lasers, which increase the likelihood of 2-photon excitation by making photon arrivals at the retina more concentrated in time. Adaptive optics provides another avenue for enhancing the 2-photon effect by focusing light more tightly at the retina, thereby increasing the spatial concentration of incident photons. This chapter makes three contributions. First, we demonstrate through color matching experiments that an adaptive optics correction can provide a 25-fold increase in the luminance of the 2-photon effect – a boost equivalent to reducing pulse width by 96%. Second, we provide image-based evidence that the 2-photon effect is most visible when light is focused at the photoreceptor level. Third, we use our results to predict the specifications for a system that could utilize 2-photon vision and adaptive optics to image and stimulate the retina using a single IR wavelength and reach luminance levels comparable to conventional displays.

2.1 Introduction

Due to the spectral sensitivities of human cone photoreceptors, wavelengths of light outside of the visible range spanning from approximately 400 to 700 nm are largely imperceptible to humans [8, 9]. However, human sensitivity to infrared light under certain viewing conditions has been observed since the mid-20th century [50, 51, 52, 53, 54, 55]. This infrared light also did not appear *red* when observed; rather, many noted that it was similar in appearance to light at half its wavelength. This observation pointed to a 2-photon process occurring somewhere in the eye. Some hypothesized that second harmonic generation was taking place

at the cornea, generating photons of visible light which could then be detected at the retina [56]. More recently, it was shown through electrophysiological experiments that 2-photon vision is the result of direct photoisomerization in the chromophores [49].

The process of 2-photon absorption has been well-characterized for its use in fluorescence microscopy. This phenomenon requires 2 photons to arrive at the same excitable molecule simultaneously. Thus, it depends greatly on the spatiotemporal density of incoming photons. Under diffraction-limited conditions, the number of 2-photon absorptions n_a generated when using a pulsed laser is dictated by

$$n_a \propto \frac{p_0^2 \, NA^4}{\tau_p} \tag{2.1}$$

where p_0 is the average laser power, NA is the numerical aperture of the focusing element, and τ_p is the pulse duration [57]. Thus, there are multiple avenues for boosting the number of 2-photon absorptions in order to make the 2-photon effect more visible. Because the uncorrected human eye does not typically have diffraction-limited optics, prior work has focused on enhancing 2-photon vision by decreasing τ_p through the use of short-pulsed lasers, or by increasing the laser power p_0.

Fortunately, adaptive optics (AO) has matured to the level where we can correct the eye's aberrations, allowing us to leverage the numerical aperture parameter NA [30]. AO allows us to use the largest physiological pupil sizes and achieve high spatial concentration of photons at each photoreceptor, effectively increasing NA and further enhancing the 2-photon effect, so that the same light can be made visible with AO while being almost invisible without it.

Others have probed characteristics of 2-photon vision including acuity [58] and contrast sensitivity [59], as well as the factors influencing it such as pulse duration [60]. However, the benefits of an AO correction on 2-photon vision have not yet been studied. In order to characterize these benefits, we carry out color and luminance matching experiments which help demonstrate the boost that AO provides in the salience of the 2-photon effect. We supplement these results with predictions about AO's enhancement of 2-photon vision, using a simple model of light capture by a hexagonal mosaic both with and without aberrations present. We are also able to collect images of the retina at varying levels of defocus which we combine with our perceptual results to establish a link between the best focus for the photoreceptors and the brightest 2-photon effect, building on the work done in (Gorczynska I, et al. IOVS 2022;63:ARVO E-Abstract 4447 – F0126) and (Doyle H, et al. IOVS 2022;63:ARVO E-Abstract 4551–F0465).

Since its discovery, 2-photon vision has generated interest for its use in clinical applications such as microperimetry for testing visual function [61, 62, 63, 64, 65, 66]. Because infrared light is less prone than visible light to scattering from opacities in the eye's optics, the 2-photon effect is potentially useful for testing visual function in ageing or precataractous eyes. Further, due to the 2-photon effect's quadratic dependence on power, the effective cone sensitivity functions are steeper, yielding a higher degree of certainty when measuring detection thresholds.

Our interest in 2-photon vision is for the entirely separate application of display technology, and especially for displays which simultaneously image and stimulate the retina [37, 43]. Such displays typically image using barely-visible infrared light and stimulate simultaneously using visible wavelengths. The infrared images of the retina are often used to inform the delivery of gaze-contingent stimuli at visible wavelengths. This multi-wavelength operation is susceptible to errors introduced by transverse and longitudinal chromatic aberrations. Both must be corrected in order to deliver light at visible wavelengths to precise locations on the retina when using an infrared image for tracking [67]. However, the 2-photon vision phenomenon means that infrared wavelengths can be made visible under certain conditions and invisible otherwise. This means that a display could be conceived which uses the same infrared wavelength for both invisible imaging and visible stimulation, thereby eliminating the aforementioned chromatic aberration challenges associated with the current paradigm. We use the results from our color and luminance matching experiments to propose a system that uses AO combined with short pulses to achieve 2-photon stimulation with a luminance that is similar to conventional displays while satisfying ANSI standards for safe power levels at the eye.

2.2 Methods

The human subjects protocol was reviewed and approved by the University of California, Berkeley Institutional Review Board and adhered to the tenets of the Declaration of Helsinki regarding ethical treatment of human subjects for research. Six subjects participated in total, four of which are co-authors of the study from which this chapter has been adapted [68]. Each provided informed consent before participating. All subjects self-reported to have no ocular disease or condition that might affect imaging. All subjects were dilated and cyclopleged using one drop of 1% tropicamide and one drop of 2.5% phenylephrine. For all experiments reported here, light exposure levels were kept within the maximum exposure limits as specified by the Z136.1 ANSI standard for the Safe Use of Lasers [69].

We carried out experiments using an Adaptive Optics Scanning Light Ophthalmoscope (AOSLO). More details of the system are provided in other work [29, 22, 70] and in Chapter 1; thus, only the most relevant aspects of the system will be described here. In the AOSLO, light was delivered in a raster-scanned pattern over a 0.9° x 0.9° square field across the retina. For the experiments done at 1064 nm, a ∼60-Hz frame rate with 256 lines per frame was achieved with a combination of a slow galvanometer scanner at 60 Hz and a fast resonant scanner at ∼16 kHz. For experiments done at 940 nm, the slow galvanometer scanner was operating at 30 Hz for a ∼30-Hz overall frame rate. The fast resonant scanner operates in a sinusoidal fashion which causes it to move more slowly at the left and right edges of the raster, resulting in brighter bands at those edges. In order to achieve a more uniformly bright appearance for ease of color matching, we centered a beam block at the retinal plane in the optical path which eliminated these bright edges. The focused spot was corrected to near diffraction-limited using AO, which is a set of optical methods to measure and

compensate ocular aberrations [30]. In this system, the wave aberrations were measured with a custom-built Shack-Hartmann wavefront sensor and the aberrations were corrected with a 97-actuator deformable mirror (DM97-08; ALPAO, Montbonnot-Saint-Martin, France). The AO ran continuously in closed-loop during all AO-corrected conditions. For AO-off conditions, the deformable mirror was set to a precalibrated 'flat-state'.

The current AOSLO can operate with up to four wavelengths scanning independently or simultaneously. All light sources were drawn from a supercontinuum laser (SuperK Extreme; NKT Photonics, Birkerod, Denmark) and coupled into four single-mode fibers. Specific wavelengths for each channel were selected by placing spectral filters into the optical path prior to fiber coupling. For the experiments reported here, narrowband filters centered at either 1055 nm [FWHM BW = 85.5 nm] or 940 nm [FWHM BW = 21.9 nm] were used in the first channel for 2-photon stimulation (reasons for using these wavelengths are given in later sections). Although we used a filter that is centered at 1055 nm, the spectrum of our supercontinuum light source contains a peak at 1064 nm, so the transmitted light was dominated by 1064-nm light. Wavefront sensing was also done with the same 940- or 1064-nm wavelengths. A second near-infrared channel with light centered at 840 nm [FWHM BW = 21.1 nm] was used to facilitate tracking and imaging (see below). The final two channels had wavelengths centered at 532 [FWHM BW = 23.9 nm] and 680 nm [FWHM BW = 29.8 nm] and were used for color matching. The power of each visible channel could be adjusted using computer-controlled acousto-optic modulators. The light in all four channels could be shut off completely using electronically activated physical shutters in their respective optical paths.

The light from the supercontinuum laser comprises short 'chirped' pulses at a repetition rate of 100 MHz, whose frequency components are spread in time. The pulse width depends on the wavelength and the bandwidth and were measured experimentally to be 14.4 ps for the 1064-nm waveband and 8.0 ps for the 940-nm waveband. These pulses, although quite long relative to the femtosecond-scale pulse widths used for 2-photon fluorescence imaging, were short enough to elicit 2-photon vision, especially with the addition of AO.

Experiments showing defocus dependence, power dependence, and AO boost (1064 nm)

The first set of experiments were done using light centered at 1064 nm. This wavelength was chosen for two reasons. First, our supercontinuum light source had a lot of available power at this band, which enabled a measurement of the power-squared dependency of the 2-photon effect. Second, the peak spectral sensitivity of the eye lies close to half of this wavelength, making the 2-photon effect especially visible. To match color and luminance, subjects used a combination of 532-nm and 680-nm light which was also delivered using the AOSLO (see above). Thus, the 2-photon field and matching fields were positioned at the same point in space, and were alternated in time as depicted in Figure 2.1a. The shutters were used to switch between the two fields every 2 seconds while the subject adjusted the mixture of 532-

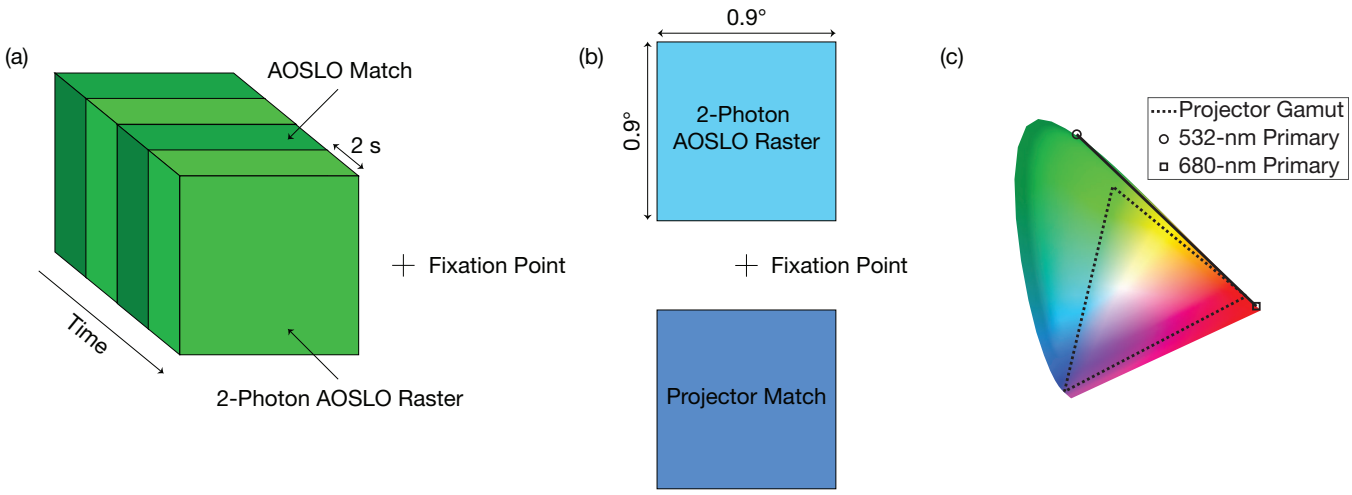

Figure 2.1: **Color matching experiment details.** (a) The 1064-nm 2-photon AOSLO raster alternates in time with an AOSLO-generated matching raster. The matching raster is a mixture of 532- and 680-nm light, which subjects tune until it is indistinguishable from the 2-photon raster. (b) The 940-nm 2-photon AOSLO raster is a 0.9° x 0.9° field positioned 0.675° above fixation. Subjects tune the color of an equally-sized projector-generated square that is positioned opposite their fixation in order to achieve a match to the appearance of the 2-photon raster. (c) The 532-nm and 680-nm primaries used in 1064-nm experiments are shown on the chromaticity diagram. The line connecting them represents all possible mixtures of the two. The gamut of the projector used for matching in 940-nm experiments is also shown, where the 3 vertices of the triangle correspond to its red, green, and blue primaries.

and 680-nm light in order to achieve a match to the 1064-nm raster. Subjects adjusted the relative proportions of 532- and 680-nm light using the motorized faders on a MIDI controller (Behringer X-Touch Compact, Willich, Germany). To obtain quantitative measures of the luminance for the matches, we multiplied the measured total power of the 532- and 680-nm sources by the fractional intensity levels chosen in a given match and computed equivalent luminance considering the field size on the retina using methods described in the appendix of [71].

Through-focus profiles of the 2-photon effect were collected by instructing subjects to make color and luminance matches to the IR raster pattern for a range of defocus settings, which were set by adding defocus offsets to the deformable mirror. The defocus settings were not uniform, but were more closely spaced around best focus to capture the maximum response in greater detail. This “best focus” was estimated prior to the beginning of the experiment, using a procedure where subjects adjusted defocus using a dial on the MIDI controller to maximize the luminance of the 2-photon effect. Each subject made 3 color

matches at 11 defocus levels, which were presented in a pseudorandom order. The power at 1064 nm for these experiments ranged from 921 to 927 μW for 4 out of 5 subjects. For the 5th subject, 20230R, the power was 837 μW due to technical limitations.

The power dependence of the 2-photon effect and the boost due to AO were measured by instructing subjects to make color and luminance matches for a range of 5 uniformly distributed power settings ranging from 81 μW to 795 μW at the eye. These power levels were achieved using neutral density filters and presented in a pseudorandom order. For these experiments, subjects first adjusted the defocus offset added to the deformable mirror to optimize for the luminance of the 2-photon effect both with and without AO. These two defocus settings were then maintained during the subsequent matching.

Experiments confirming that 2-photon effect occurs at the photoreceptor layer (940 nm)

The second set of experiments were done with light centered at 940 nm, chosen because there were detectors commercially available to perform imaging along with the color and luminance matching. Subjects matched to the 0.9° AOSLO raster using a similar-sized square generated by a DLP LightCrafter projector (Wintech, Carlsbad, CA) that was coaligned with the AOSLO. The projector display had a total field of view of ∼18 degrees and was viewed through a Badal optometer configuration which enabled the defocus setting for each individual to be adjusted and for which all the light from the projector was delivered into the eye via a ∼7-mm exit pupil that was coaligned with the exit pupil of the AOSLO (this is often referred to as a Maxwellian view). The projector display was programmed using MATLAB (Mathworks, Natick, MA) with the Psychophysics Toolbox [72, 73, 74] to present calibrated RGB images to the subject. In this experiment, subjects saw two squares positioned on opposite sides of a fixation cross as shown in Figure 2.1b. The fixation cross and matching square were generated by the projector and the 2-photon square was generated by the AOSLO's raster scan. Subjects adjusted the RGB values of their projector-generated matching square using the motorized faders on the MIDI Controller.

The projector display was configured in Maxwellian view, making direct measurements of its radiometric properties challenging. To obtain quantitative measures of the luminance for the projector matches, we first used a spectroradiometer (PR650, PhotoResearch (now Jadak), North Syracuse, NY) to measure the shape of each primary's spectral power distribution. We then empricially measured the responsivity of our optical power meter (Newport, Irvine, CA) and used that power meter to measure the power of each primary at its maximum intensity setting. Using these measurements, we could infer the scaling factor which converted the spectra measured by the spectroradiometer into absolute units of power. Taking into account the field size on the retina, we could then compute the luminance of any linear combination of the projector's primaries.

At 940 nm, we also wished to collect images of the subjects' retina. To do this, we placed a 90:10 beamsplitter in the path of the wavefront sensor and collected the diverted light

using an avalanche photodiode (APD410A/M, Thorlabs, Newton, NJ) in order to generate an image. Due to the fact that the power was low and the sensitivity of the detector was not ideal, we needed to average several 940-nm images together in order to achieve a high enough signal-to-noise ratio for the image. To facilitate frame averaging, we simultaneously tracked the eye motion by imaging at 840 nm and used this to stabilize the incoming 940-nm images for averaging. As a result, we were limited in the defocus range that we could image over, because we lost signal in 840 nm as we went more out-of-focus and could no longer track. As the 840-nm light used for imaging was readily visible, the imaging was done alternately, but not simultaneously with the color and luminance matching. During the color and luminance matching, the shutter was used to block the 840-nm channel entirely.

All 940-nm experiments were done with AO correction. As in the 1064-nm experiments, varying levels of defocus were added to the deformable mirror in order to collect a through-focus profile of the 2-photon effect where the spatial confinement of the raster-scanned spot was varied. Each subject made 3 color matches at 11 defocus levels, which were presented in a pseudorandom order. The power at 940 nm ranged from 206 to 209 μW across 5 sessions.

Modeling

To confirm that the results were consistent with expectations, we performed simple modeling to predict the increases in 2-photon luminance that we would expect with defocus and aberration correction via AO. We modeled this using custom code written in MATLAB.

In this model, we iterated through defocus levels ranging from -1 D to 1 D in increments of 0.01 D. At each defocus, we computed the PSF of 1064-nm light at the retina resulting from the added defocus combined with the aberrations of the eye. After the PSF was computed, we applied a binary mask intended to mimic light collection by a cone mosaic. This mask consisted of cones which were modeled as circles with a radius of 0.5 arcmin in a close-packed hexagonal arrangement that extended over the entire field size of the simulation, which was 66.9 arcmin. Because the number of 2-photon absorptions increases with the square of light intensity as dictated by Equation 2.1, we took the squares of the integrated PSF intensity for all cone apertures in the mask and summed them to produce a proxy for 2-photon luminance.

In order to evaluate the boost in 2-photon luminance provided by an AO correction, we ran this model for an ideal, aberration-free eye and compared it to results using real aberration data. We used Zernike coefficients from 10 de-identified adult human subjects (mean age: 26.3 $\pm$ 4.3 years; range: 22–34 years) with a 7-mm or greater pupil size. These subjects were taken from a previously published dataset which included 74 human eyes [75]. For the purposes of our modeling, the 10 subjects were uniformly drawn from the larger dataset ordered by high-order RMS, avoiding the extremes.

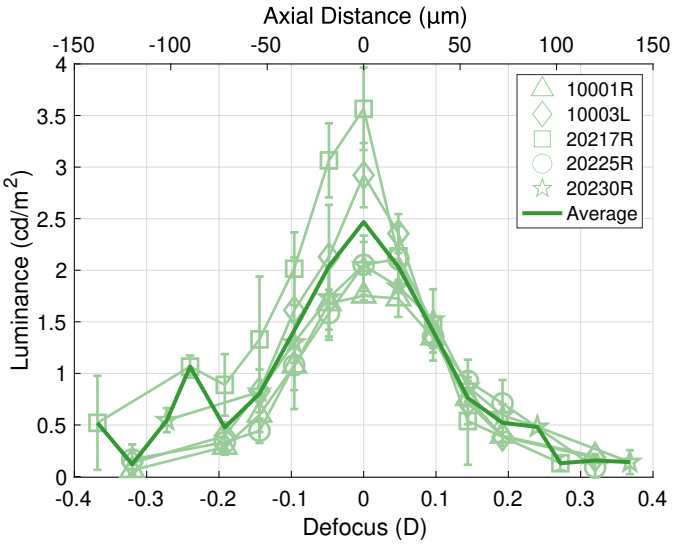

Figure 2.2: **Through-focus 2-photon luminance profile at 1064 nm.** Subjects made 3 matches using a mixture of 532- and 680-nm light at each of the 11 defocus levels. The total luminances of their matches are plotted against defocus and axial distance in microns. We fit a Gaussian to each subject's data and center the closest sample to the Gaussian's peak at 0 D for ease of comparison between subjects. The matched luminance of the 2-photon effect peaks around an optimal focus for each subject.

2.3 Results

Human experiments

Color and luminance matching results for the 1064-nm and 940-nm experiments described above are presented in order below.

at 1064 nm

The through-focus luminance profiles of the 2-photon effect at 1064 nm for each subject are shown in Figure 2.2. For these experiments, the amount of 1-photon isomerization of 1064-nm light is negligible – the 680-nm luminance decreases to 0.018 cd/m^2 on either defocus extreme, on average. The 680-nm component also rises with the 532-luminance component as the focus changes, suggesting that both are necessary in order to match the color appearance of the defocus-dependent 2-photon effect. Thus, we plot the combined luminance of both the 532-nm and 680-nm components in Figure 2.2 to represent the 2-photon effect's total luminance.

We can calculate the equivalent wavelength that is metameric to each match combination, as we know the proportions of 532- and 680-nm light along with their absolute power levels.

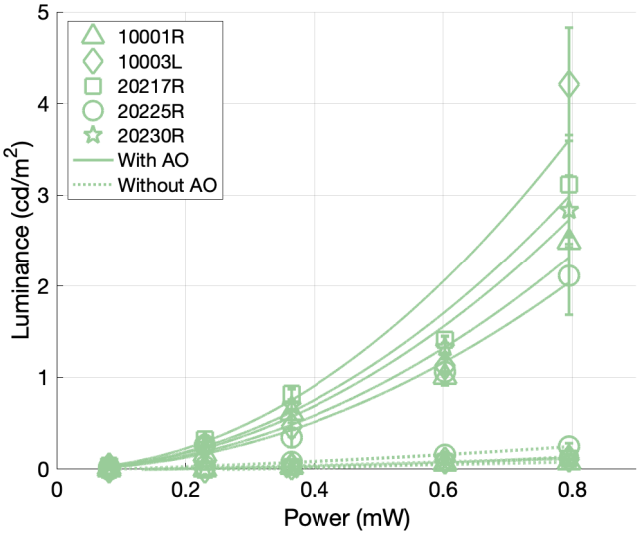

Figure 2.3: **Power dependence of 2-photon luminance with and without an AO correction.** Subjects made 3 matches with AO and 3 matches without AO to the 1064-nm 2-photon raster at 5 laser power settings. The total luminances of their matches are plotted against laser power. We fit a quadratic model to the luminance results with and without an AO correction. The matching results show a significant boost in 2-photon luminance as a result of AO, with the boost for each subject ranging from 8.5x to 36.8x at the highest power setting.

In doing so, we find that the average through-focus equivalent monochromatic wavelengths are 542 nm, 544 nm, 553 nm, 554 nm, and 558 nm across our 5 subjects. Thus, the color appearance of the 2-photon effect at 1064 nm tends to skew toward wavelengths that are longer than the expected half-wavelength of 532 nm. In these results, we also see that the luminance of the 2-photon effect decreases on either side of the optimal focus for each subject, which was determined psychophysically at the start of the experiment. We will later show through imaging results at 940 nm that this optimal focus corresponds to the defocus setting where light is focused most tightly at the layer of the photoreceptors.

We also investigated the power dependence of the 2-photon perceived luminance with and without AO at 1064 nm. Subjects again matched by tuning a mixture of 532- and 680-nm light, and the total luminance of their matches at 5 power levels is plotted in Figure 2.3. We see that the luminance of the 2-photon effect varies with the square of the laser power, as expected. For all subjects, there is a significant boost in luminance when AO is used. This boost ranges from 8.5x to 36.8x at the highest power level, with an average increase of 25.5x when using AO. These results establish conditions under which nearly invisible infrared light can be made visible through the use of AO alone.

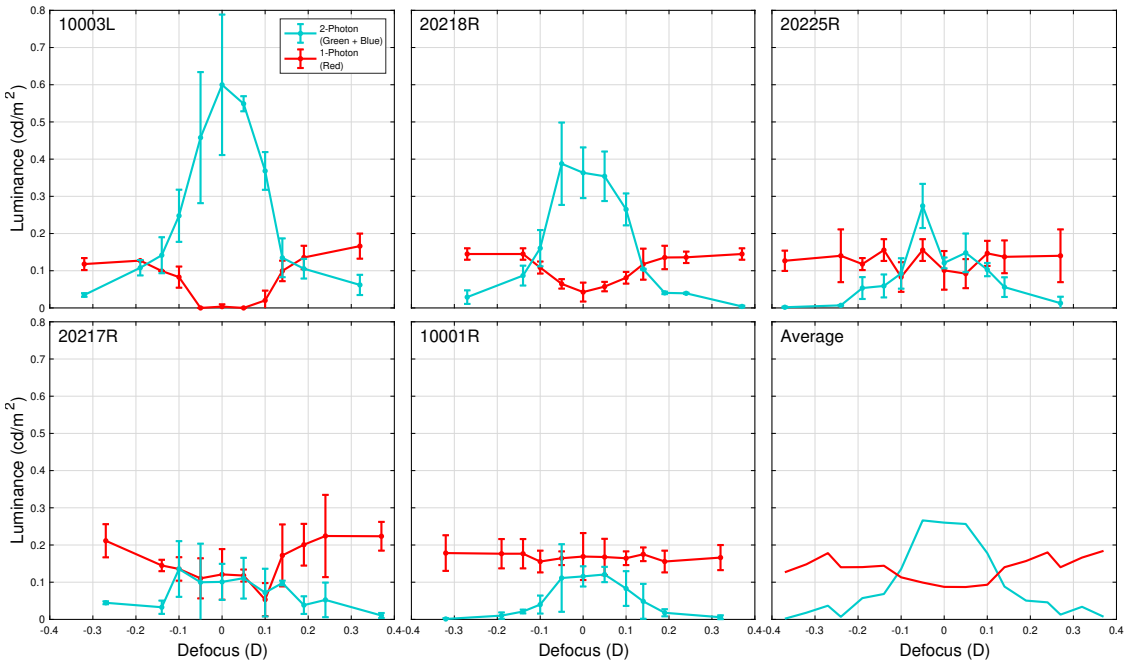

Figure 2.4: **Through-focus 2-photon luminance profile at 940 nm.** Subjects made 3 matches using an RGB projector to the 940-nm 2-photon raster at 11 defocus levels. The red component and the combination of the green and blue components of their matches are plotted as luminance for each defocus. The green and blue mixture is taken to represent the luminance of the 2-photon effect at 940 nm, which increases around an optimal focus for each subject. Each subject's data is aligned for comparison using the same procedure as in Figure 2.2.

at 940 nm

For experiments at 940 nm, there is a non-negligible visible red component due to 1-photon isomerizations of 940-nm light in addition to the 2-photon effect. Thus, in Figure 2.4, we separate this 1-photon component from the 2-photon component of the match made using an RGB projector. The 1-photon isomerizations should appear to be a pure red as they would only stimulate long-wavelength sensitive cones, so we take the red value of the RGB match to represent the 1-photon component entirely. The fact that the red luminance persists and remains relatively flat and consistent between subjects at the limits of the defocus range is evidence that the red primary encodes 1-photon isomerizations. The 2-photon component can then be explained by the remaining combination of the green and blue projector primaries. These RGB values are converted to luminance and plotted in Figure 2.4 at each of the 11 defocus levels. We again see that there is an optimal defocus level around which the luminance of the 2-photon effect peaks for each subject, as it did in

our experiments at 1064 nm.

It is also apparent that the red component appears to be anticorrelated with the green and blue components, especially for subjects 10003L and 20218R. That is, there is a decrease in the red component around defocus values where the 2-photon component is dominant. This cannot be due to a reduction in 1-photon isomerizations. Rather, we surmise that it is because matching was done using a projector, and subjects were limited in the gamut of colors that could be achieved with the matching stimulus, as shown in Figure 2.1c. As a result, some subjects could not achieve the same saturation on the matching stimulus as they saw in the 2-photon stimulus, and instead opted to decrease the red component of their RGB match in an attempt to compensate, at some cost to the fidelity of the overall match.

The use of AO also made it possible to collect images at 940 nm with the same channel that was used for 2-photon stimulation. For each subject, we collected images for at least 4 defocus settings around the best focus. In Figure 2.5, we compare the images collected at each defocus level to the corresponding average match luminances across all subjects. We see that the optimal focus for maximizing 2-photon luminance is at or near the optimal focus for sharp images of the photoreceptors. This correlation is more apparent for some subjects than others; as noted before, we relied on simultaneous tracking using 840-nm imaging in order to frame-average images in 940-nm due to low signal and low photodetector sensitivity to 940 nm. Unstable tracking could cause the 940-nm image SNR to suffer, or it may have prevented us from collecting an image entirely, as is the case for subjects 10003L, 20217R, and 20225R at certain defocus levels. Nevertheless, we do tend to see sharper photoreceptor structure in images near the defocus level where 2-photon luminance is highest. Indeed, the imaging results suggest that the optimal focus for imaging the cones is at least within $\sim$25 microns axially from the optimal focus for 2-photon luminance. That is, the 2-photon luminance is increased when light is focused near the photoreceptors. This provides imaging-based support for the finding that the 2-photon absorptions are occurring at the photoreceptors and that 2-photon vision is the result of direct 2-photon isomerization of cone photopigments.

Modeling

The results of our modeling for the luminance of the 1064-nm 2-photon luminance are shown in Figure 2.6. There is a significant boost in the modeled 2-photon luminance of the AO-corrected ideal eye over the aberrated eyes. This boost ranges from 9.0x to 35.1x between the peaks of the aberrated eyes and the ideal eye, with an average of 20.1x. For comparison, the average boost from AO found in our experiments was 25.5x, ranging from 8.5x to 36.8x among the 5 subjects in experiments at 1064 nm. That the boost is slightly smaller in modeling on average may be due to our method for finding optimal focus prior to carrying out the color and luminance matching. Subjects used a dial on the MIDI controller to change the defocus setting until they found the brightest 2-photon effect both with and without AO. Because the luminance without AO was so low, subjects may not have been sensitive enough to tune the defocus to its truly optimal setting. This would have resulted in an inflated boost

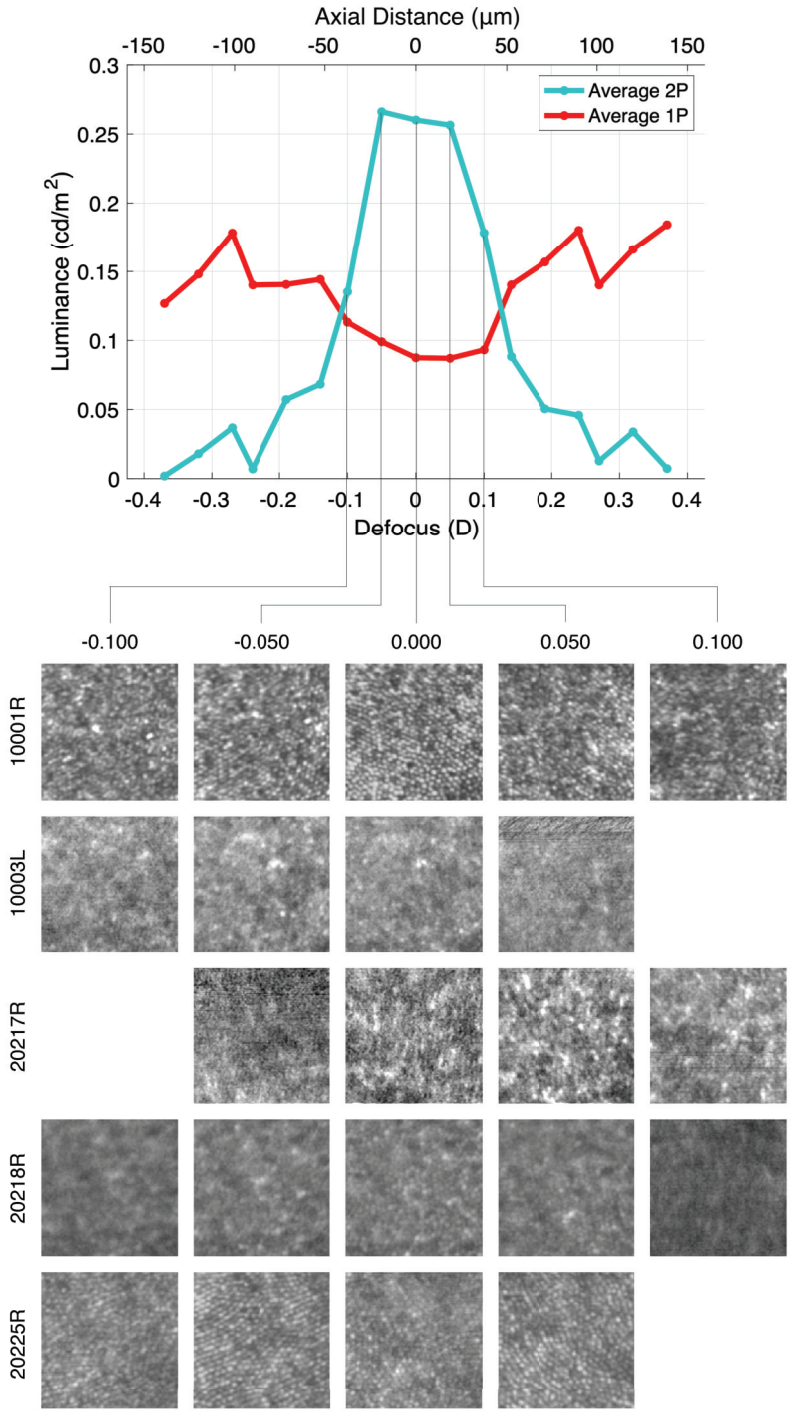

Figure 2.5: **Imaging results and corresponding 2-photon luminance data at 940 nm.** Images were collected at the defocus levels where subjects made matches. The central thirds of each subject's images are shown in separate rows, with each column corresponding to a given defocus level. Lines connect each of the defocus levels to the corresponding point in the plot of average 2-photon luminance across all subjects. The sharpest images of the photoreceptors tend to coincide with the brightest matches.

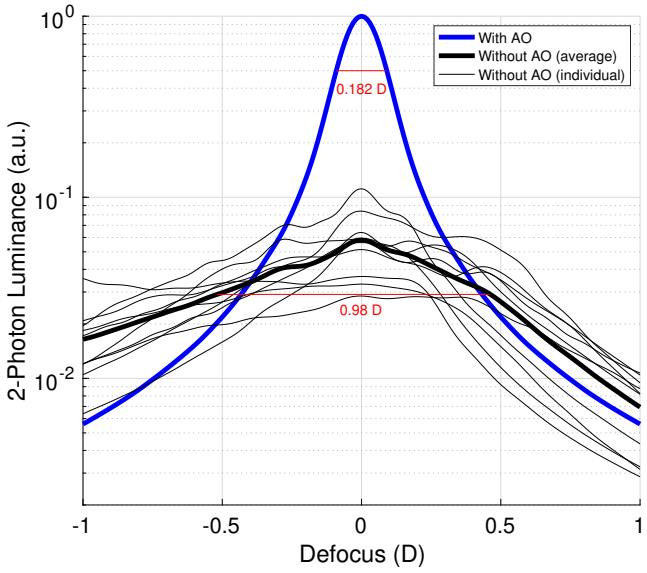

Figure 2.6: **Modeling of through-focus 2-photon luminance profile and boost from AO.** The blue line is the simulated 2-photon luminance on a log scale (arbitrary units) vs. defocus for a perfect AO correction. The thin black lines are the simulated 2-photon luminances for 10 eyes with varying types and degrees of aberration. The thick black line is the average of these uncorrected eyes. All modeling results are normalized so that the ideal eye peaks at 1 a.u. and aligned so that all peaks are at 0 D. The FWHMs of the with- and without-AO plots are labeled in red.

between the AO on/off cases relative to the modeling, where boost factors are calculated using the true optimal defocus setting for each real eye.

The full width at half maximum (FWHM) of the luminance vs. defocus plot for the eye with an ideal AO correction is 0.182 D (68.3 μm). We can compare this to our own results by fitting a Gaussian to all subjects' luminance vs. defocus data from Figures 2.2 and 2.4. In doing this, we find that the FWHM of our subjects' data is 0.243 D (91.1 μm) and 0.221 D (83.0 μm) for 1064 nm and 940 nm respectively. For comparison, the FWHM of the average non-AO-corrected eye's luminance vs. defocus in our modeling was found to be 0.980 D (367.5 μm). Thus, the FWHM values found in our data agree more closely with the modeled luminance under an AO correction, as expected.

2.4 Discussion

Future system specifications

We have shown that AO can be used to create a strong 2-photon effect without the need for ultrashort, femtosecond-scale pulses. A system that combines short pulses with AO would then reach even higher luminance levels that are comparable to conventional displays. Our results establish a benchmark and can be used to inform the specifications for the development of displays based on 2-photon vision, which would eliminate the chromatic aberration challenges associated with gaze-contingent displays that image with IR and stimulate with visible light. If we take the average luminance at the highest laser power from Figure 2.3, we can extrapolate using the quadratic power dependence to determine the power required to achieve a desired display luminance. Combining this with a reduction in pulse duration using Equation 2.1, we can reach even higher luminances with reduced power. In doing so, our data suggests that a 500-cd/m^2 display could be achieved with an average power of 0.86 mW and a pulse duration of 100 fs with the addition of an AO correction. Several candidate lasers for such a system already exist, with wavelengths close to 1064 nm and pulse widths close to 100 fs [76, 77, 78]. In such a system, the femtosecond source would be used for stimulation, appearing like a monochromatic source around half of its IR wavelength. A continuous-wave source at the same IR wavelength would then serve as the imaging light while remaining nearly invisible due to its low temporal concentration. This imaging and stimulating system would enable precise, single-cone level retinal stimulation without the careful correction of chromatic aberration that would typically be required. In implementing such a system, we must also ensure that exposures are kept at safe levels.

Performing experiments in the AOSLO system also allowed us to image using the same wavelength channel that was creating the 2-photon effect, so that retinal imaging could be done along with our psychophysical experiments. We were thus able to show that the 2-photon effect's luminance increased when light was focused at the photoreceptors, providing further support for the finding that 2-photon vision is a result of direct excitation of cone photopigments. This result is an added benefit for any future system that combines IR imaging with 2-photon stimulation, as the optimal focus for imaging the cones will coincide with the optimal focus for precise stimulation of the cones. This is often not the case in systems which use separate wavelength channels for imaging and stimulation due to the presence of longitudinal chromatic aberrations (LCA) in the eye's optics, which varies across subjects. In a multi-wavelength system, this inter-subject variability in LCA requires custom compensatory solutions that add complexity to system design [79].

Color appearance

In doing color matching experiments, we found that the color appearance of the 2-photon effect at 1064 nm was not exactly matched by 532-nm light alone, which would correspond to half of the IR wavelength. Rather, subjects found it necessary to add some amount of

680-nm light in order to achieve a match to the 2-photon effect. As discussed previously, this is unlikely to be due simply to 1-photon isomerizations of 1064-nm light, as we found a focus dependence in the red component. That is, the added 680-nm component rose and fell in a way that was correlated with the green 532-nm component. This suggested instead that there was a redshift in the 2-photon effect's color itself relative to the expected half-wavelength appearance.

In calculating the average through-focus equivalent wavelength, we found a mean of 550 nm and standard deviation of 6.8 nm across our 5 subjects. The origin of this redshift phenomenon in the 2-photon effect is unclear, but it has been observed before in color matching experiments [49]. One possible explanation is that the 2-photon cross section may differ between cone types, resulting in a change in the realized color appearance relative to what would be predicted under 1-photon isomerizations by light at half of the IR wavelength. If this were the case, this shift in color appearance toward redder wavelengths would suggest that L cone opsins may have a larger 2-photon cross section than M cones, thereby amplifying the L-cone activation level. Another possibility which has been suggested is that secondary absorption of slightly longer-wavelength photons emitted by a 2-photon fluorescence process in rhodopsin could lead to this redshifted color appearance [49].

Individual differences

There is a notable difference between the color matching data at 940 and 1064 nm in the degree of inter-subject variability. At 1064 nm, there is a 2-fold difference in peak 2-photon luminance. This is not too surprising, as there can be intersubject variability in the quality of AO correction, scatter, or even photoreceptor coupling efficiency.

For 940-nm, however, we see a 6-fold difference in the highest and lowest reported 2-photon luminances. We hypothesize that this disparity could be explained by variation in macular pigment concentrations between subjects. Although macular pigment concentrations can vary by a factor of >10 across the population [80], people generally agree on the blueness of objects in the world under normal viewing conditions. As such, they must have developed a post-receptoral amplification factor which compensates for the attenuation of blue signals by their own macular pigment density, as suggested by [81]. However, 2-photon stimulation by 940-nm light presents a unique scenario where the incoming light is not actually attenuated by macular pigment, yet it stimulates as if it were light near 470 nm. The resulting blue signal should therefore be subject to the same adaptive factors that would affect blue light under normal viewing conditions. Since those adaptive factors vary between people, the blueness and brightness of the 2-photon effect could be amplified to different degrees perceptually. These different amplification factors could explain the wide variation across subjects who are matching to the same 2-photon stimulus. It is also consistent with the reduced inter-subject variation in the experiments at 1064 nm, which would not be affected by the same post-receptoral amplification, as 532-nm light is virtually unabsorbed by macular pigment [82]. Thus, we would expect more variation between subjects in the data collected at 940 nm due to differences in their macular pigment concentrations and resulting

compensatory factors. Future work will seek to validate this hypothesis by supplementing the color matching results with objective measurements of macular pigment optical density in each subject.

2.5 Conclusions

In prior work, the 2-photon effect in vision has been made more salient using lasers with pulses on the scale of femtoseconds. With this work, we have shown that a boost in 2-photon luminance can instead be provided by an AO correction, through its ability to focus light tightly at the level of the photoreceptors. We used color and luminance matching experiments at 1064 nm and 940 nm to characterize the through-focus luminance profile and laser-power dependence of the 2-photon effect. The use of an AO correction yielded a 25-fold boost in 2-photon luminance, on average. We supplemented these results with a model of the through-focus 2-photon luminance profile with and without AO, and found a predicted boost factor and FWHM which resembled our experimental results. We used the same infrared channel that generated the 2-photon visual sensations to collect images at several defocus settings, which revealed that the 2-photon effect appeared brighter as the image of the cones became sharper. This provided image-based evidence that the 2-photon effect indeed occurs in the cones.

The phenomenon of 2-photon vision has previously been explored primarily due to its potential for testing visual function in clinical settings. With this work, we have proposed a new application for 2-photon vision: a display system that can image and stimulate the retina using one IR wavelength. Such a display would have the following benefits: First, it would eliminate the need to account for the effects of chromatic aberration between channels in a multi-wavelength system. Second, the power-squared dependence of the 2-photon effect means that any 2-photon stimulation would have increased contrast as compared to the background 1-photon imaging light. Third, the defocus dependence of the 2-photon effect means the optimal focus for sharp imaging would coincide with the optimal focus for stimulation luminance. We have extrapolated from our 2-photon luminance measurements in order to specify the pulse duration and power required to achieve a 500-cd/m^2 display using 2-photon stimulation with AO, and verified that such a system is achievable with current technology. Future work may involve the development and testing of this kind of display system.

2.6 Acknowledgments

This chapter was published as a paper with co-authors Sofie R. Herbeck, Alexandra E. Boehm, John E. Vanston, Ren Ng, William S. Tuten, and Austin Roorda [68]. The authors thank NKT Photonics for providing pulse width measurements for the supercontinuum laser used in these experiments. This work was supported by the following grants: Air Force Office of Scientific Research Awards FA9550-20-1-0195 & FA9550-21-1-0230; Bioengineering

Research Partnership Grant, National Institutes of Health: R01EY023591; Center Core Grant, National Institutes of Health: P30EY003176; and Training Grant, National Institutes of Health: T32EY007043.

Chapter 3

Novel Color via Stimulation of Individual Photoreceptors at Population Scale

Human color vision is derived from the relative activation levels of the three cone types present in the retina. These activation levels are dictated both by the spectral makeup of incident light and by the spectral sensitivity profile of each cone type. Because there is overlap among the spectral sensitivity profiles of the three cone types, their activations are correlated with one another. This correlated behavior constrains the number of activation patterns that are possible across the three cone types, thereby limiting the gamut of color sensations that are achievable for humans. Here we present Oz, a principle for displaying color imagery that uses cell-by-cell light delivery to stimulate each cone type independently, breaking this correlation between their activation levels. We show through color matching experiments that this cone-targeted stimulation allows us to produce color percepts that fall outside of the human color gamut as it had been previously defined. Our results extend the range of color sensations available to humans by generating visual stimuli which are impossible to achieve under natural viewing conditions.

3.1 Introduction

All color reproduction technology today, including RGB displays and CMYK printers, is based on *spectral* metamerism, which works by producing light of a spectral power distribution that causes the same activation level as a target color for each cone type in the retina. This approach dates back to at least 1861, when Maxwell gave a live demonstration at the Royal Institution that superimposing red, green, and blue images could produce the appearance of full-color images to human observers [83]. In this study, we introduce a fundamentally different principle for displaying color, which we call Oz, consisting of optically stimulating individual photoreceptor cells on the retina at population scale in order to di-

rectly control their activation levels. In principle, arbitrary colored visual imagery can be reproduced by this cell-by-cell approach (see Fig. 3.1). The Oz principle can be thought of as *spatial* metamerism in the sense that it is based on shaping the spatial distribution of light on the retina rather than its spectral distribution.

Oz enables fundamentally novel colors that lie beyond the natural gamut (space of colors) of human vision. For example, in normal color vision, any light that stimulates the M cones must also stimulate the L and/or S cones, because of overlap in their spectral response functions [8, 9]. Aside from spatial metamerisim, the only known ways to selectively excite M-cones has been via pre-adapting of the other cone types [84, 85, 86] which is a transient effect by definition, or by a method called silent substitution[87, 88] which can be used to modulate a single cone type, but not isolate it. However, cell-by-cell stimulation in Oz can naturally target light to only M cones and not L or S with relatively high contrast and in a sustained manner, which in principle would send a novel color signal to the brain. In principle, Oz expands the well-known, bounded color gamut of natural human vision [12] to any (L,M,S) color coordinate with non-zero elements. In practice, we achieve a partial expansion of colorspace towards this theoretical maximum, depending on the wavelength of the laser, diffraction limit, cone cell size, and computational latency errors.

We prototype a system for displaying Oz imagery to human subjects. Our system builds on previous work that pioneered cone-targeted stimulation and psychophysics of single cone cells [43, 32, 45, 44] or pairs [46]. We build our Oz prototype on an AOSLO [29] that simultaneously images and stimulates the retina with a raster scan of near-diffraction-limited laser light over a 0.9° square field-of-view. Using nearly-invisible infrared light to image the retina, we can track the eye's motion in real time. We compensate for this motion and deliver pulses of visible-wavelength laser dynamically targeted at each cone cell within the field of view. These laser microdoses are delivered at a rate of 10^5 per second to a population of 1000-2000 cones.

In order to achieve an intended LMS activation through cone-targeted stimulation, the spectral type of each cone must be known. In a preparatory step, cone cells are classified by spectral type in the subject's retina using recently-developed optoretinography techniques in an AO-OCT system [39, 41, 40]. In this study, we use a classified region containing 1000-2000 cones located near 4° eccentricity from the foveola. These regions span an area that is larger than our system's field of view, so that cones that fall within the stimulated region are classified, even under fixational eye motion.

We show Oz stimuli to human subjects and perform the following experiments: color matching of uniform Oz color squares, and alternative-forced-choice image and video recognition experiments. As a control condition, stimuli are randomly repeated with microdose delivery intentionally compromised. During these control trials, each microdose is "jittered" randomly so that it lands on a random neighboring cell. In this case, the microdose pattern delivered to the retina is no longer correlated with the subject's cone mosaic, and we expect the subject's perception of the color to converge on the color of the stimulating laser.

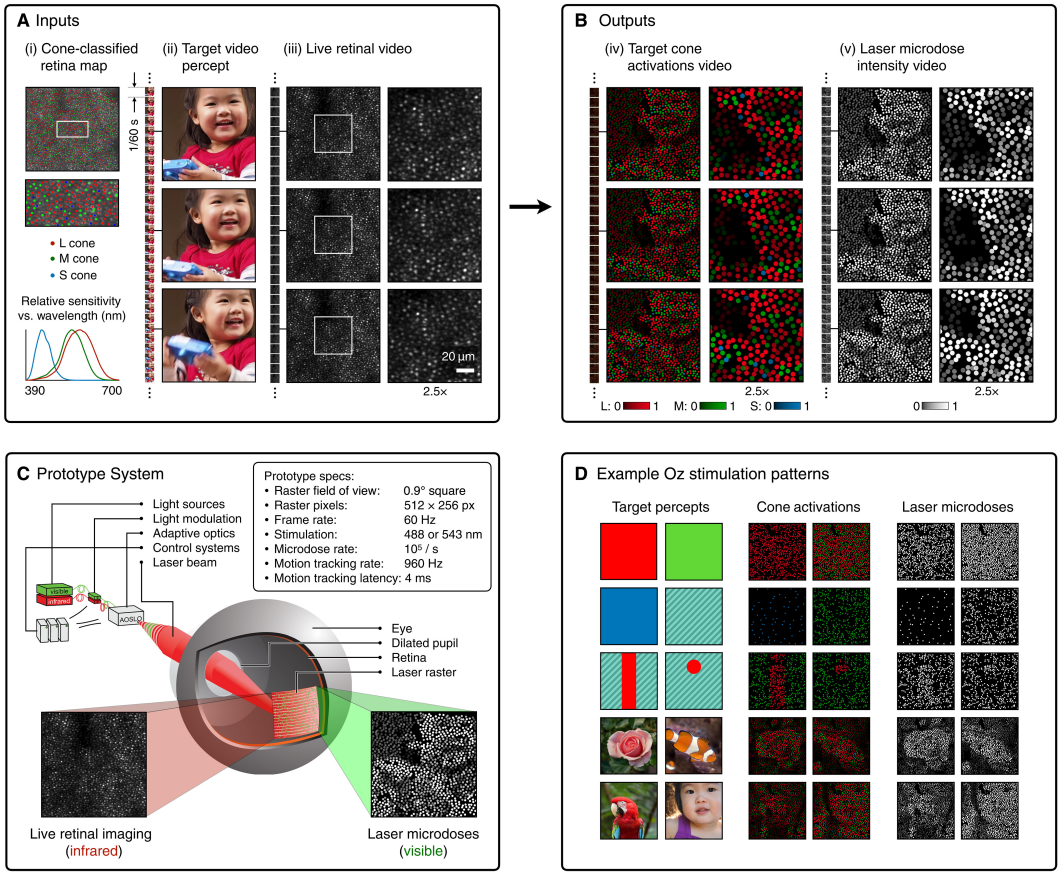

Figure 3.1: **Overview of novel principle and prototype system.** (**A**) System inputs. (i) Retina map of 10^3 cone cells pre-classified by spectral type [40]. (ii) Target visual percept. (iii) Infrared cellular-scale imaging of the retina with 60 frames-per-second rolling shutter. Fixational eye movement is visible over the three frames shown. (**B**) System outputs. (iv) Realtime per-cone target activation levels to reproduce the target percept, computed by: extracting eye motion from the input video relative to the retina map; identifying the spectral type of every cone in the field of view; computing the per-cone activation the target percept would have produced. (v) Intensities of visible-wavelength 488 nm laser microdoses at each cone required to achieve its target activation level. (**C**) Infrared imaging and visible-wavelength stimulation are physically accomplished in a raster scan across the retinal region using AOSLO. By modulating the visible-wavelength beam's intensity, the laser microdoses shown in (v) are delivered. Drawing adapted with permission (Harmening and Sincich [89]). (**D**) Examples of target percepts with corresponding cone activations and laser microdoses, ranging from colored squares to complex imagery. Teal-striped regions represent the novel color 'olo' of stimulating only M cones.

3.2 Results

Color matching experiments

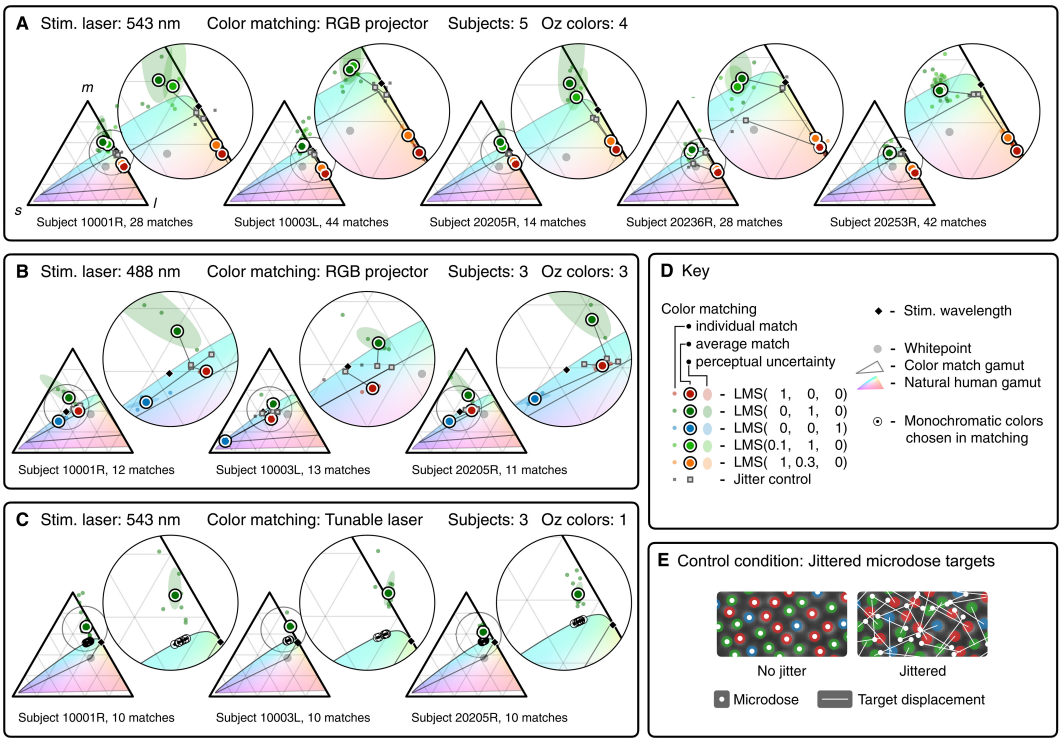

Figure 3.2: **Color matching of Oz colored squares produced by cone-by-cone stimulation.** (**A** to **D**) Each *lms* chromaticity triangle plots color matches for one subject with the indicated stimulation wavelength and type of matching color system (RGB projector, or tunable near-monochromatic laser and projector white). Target colors are specified as (L, M, and S) triplets, which are the relative light intensity levels directed to each cone class. Color matches to different target colors are denoted with differently colored markers. Each triangle also plots: color matches for randomly interleaved jitter control condition [see **E**]; coordinates of the stimulation wavelength; natural color gamut of human vision; gamut of the matching color system and its whitepoint; and perceptual uncertainty ellipses for the average color matches (projected JND ellipsoid at the coordinates of the "positive" component of the color match, computed from CIELAB/ΔE^*_{ab}, scaled three times the actual size). Ellipses not visible are smaller than their associated markers. (**E**) Illustration of the control condition randomly interleaved into all experiments: microdose target locations are randomly jittered by two intercone spacings in Oz stimuli that are otherwise identical to the experimental condition.

Fig. 3.2 graphs results of the color matching experiments. 5 subjects performed 222 color matches. We highlight four observations.

First, Oz colors form a triangle around the stimulation wavelength for 488 nm (panel **B**), and a line of colors for 543 nm (panel **A**). This is consistent with the fact that 488 nm activates all 3 cone types, whereas 543 nm primarily activates L and M cones. Second, the jitter control condition causes the color to "collapse" toward the stimulation wavelength, as expected.

Third, the variance in matching *lms* chromaticity increases with the distance of Oz colors from the gamut of the color matching system. This is a consequence of perceptual uncertainty being calculated in CIELAB at the positive match point before being translated according to the added negative color and projected onto the *lms* chromaticity triangle.

Fourth, panel **C** provides unequivocal confirmation that olo lies beyond the natural human gamut. In these matches, all subjects found it necessary to desaturate olo with projector white in order to match the (near) monochromatic colors shown, which lie on the boundary of the natural human gamut. These matching monochromatic wavelengths, from 501 to 512 nm, are the most saturated teal hues for normal color vision under the test subjects' viewing conditions.

Subjects' qualitative hue naming and saturation ratings corroborate these quantitative results. Color names volunteered for olo include "teal," "green," "blue-greenish," and "green, a little blue." Subjects consistently rate olo's saturation as 4 out of 4, compared to an average rating of 2.9 for the near-monochromatic colors of matching hue shown in row **C**.

Image and video recognition experiments

We design image and video recognition experiments to probe the ability of human subjects to understand images created with spatial metamerism in Oz. We use 4-alternative forced choice (4-AFC) and 2-AFC tasks where subjects can only succeed using hue information created through accurate Oz stimulation. In the 4-AFC task, subjects must identify the orientation of a line in a static image. In the 2-AFC task, subjects must detect the rotation direction in a video of a moving disk. In these stimuli, the lines and disks are rendered as red (all-L cone) on an olo background (all-M cone), delivered using a stimulating wavelength of 543 nm. A calibration step is performed to ensure that foreground and background are equiluminant (see Methods 3.4), so that in the jitter control condition, the square appears as a uniform square of the laser color and the task reduces to guessing.

Fig. 3.3 plots the results of the 4-AFC line orientation task and the 2-AFC rotation direction task.

In the experimental condition, subjects are able to reliably detect both line orientation and motion direction (blue bars). In the control condition (with jitter), subjects' performance is reduced to guessing for both tasks (gray bars).

These quantitative results are borne out with qualitative descriptions of the experiment. Subjects report seeing either red or orange lines and disks on a blue-green or green background, when the task was easy, compared with a uniform square of yellow-green, when they

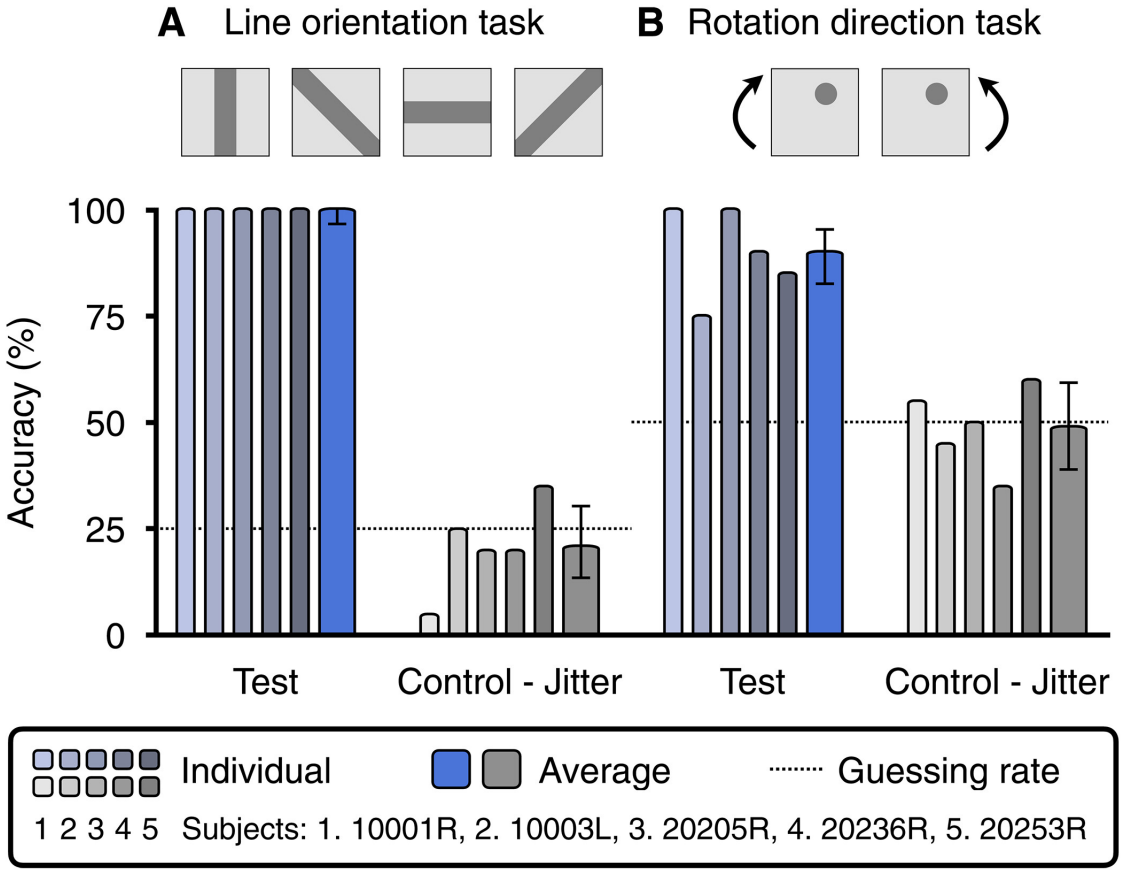

Figure 3.3: **Image and video recognition experiments.** We tested subjects' ability to recognize image and video content consisting of Oz colors: **A**, a 4-alternative forced choice (4-AFC) line orientation recognition task, and **B**, a 2-AFC rotation direction task experiments. Oz stimuli consisted of equiluminant red lines and disks presented on an olo background, as depicted. The bar graphs show individual subject performance over 20 trials per condition and average accuracy across 5 subjects with 95% confidence intervals. In experimental conditions with Oz microdoses delivered experimentally (blue bars) subjects are able to accurately identify line orientation and rotation direction. In control-group stimuli (gray bars), where cone-targeting is compromised through jittering microdose target locations, task accuracy is reduced to guessing rate as indicated by the dashed lines.

were forced to guess. The former correlates directly with accurate Oz microdose deliveries, and the latter with the jitter control condition, where only the natural color of the 543 nm light should be perceived.

3.3 Discussion

Oz represents a new class of experimental platform for vision science and neuroscience, which strives for complete control of the first visual neural layer to the brain—programmability of every photoreceptor's activation at every point in time. Our prototype and experiments offer visually-striking proof that this class of neural control is now achievable. When Oz microdoses are intentionally "jittered" by just a few microns, subjects perceive a square of just the ordinary laser color. When these same Oz microdoses are delivered accurately, subjects can be made to perceive different colors of the rainbow, unprecedented colors beyond the natural human gamut, and imagery like brilliant red lines or rotating dots on an olo background.

The fact that no ordinary light can stimulate the M cells in isolation has long been noted. Previous experiments have elicited temporary color percepts outside the natural gamut [84, 86], with methods such as bleaching L photopigment with red light before displaying green light. However, such percepts rely on fleeting adaptation states and after-images, so they are difficult to measure precisely [84, 90] and lack the spatial control for general imagery. Alternate methods delivering light to only one [43, 32, 45, 44] or two [46] M cells at a time revealed variable hues that depended on the surround conditions. In contrast to both of these approaches, spatial metamerism in our Oz prototype produces novel colors like olo stably enough and over a large enough area for color matching, for sustained durations (a minute or longer if desired), and within arbitrary colored imagery.

The required control of photoreceptor activations at population scale is technically challenging, and our experiments are limited to a field-of-view of 0.9° square centered at 4° eccentricity, which requires gaze fixation. Enlarging Oz to an apparent N° square field-of-view and relaxing the fixational requirement so that the subject can freely examine any part of the video faces significant technical challenges. It would require spectral classification of the central 2N° square patch of retina (classification has progressed to within 0.3° eccentricity, but not yet to the smallest cells in the fovea [41, 42]). It would require improving optical focus and spatiotemporal accuracy to achieve diffraction-limited microdoses within each cell, while allowing saccadic eye motion within the video field of view. It would also require scaling up; for example, to $4 \cdot 10^4$ cones and 10^7 microdoses per second for a 2° × 2° "free-gaze" Oz system.

Spatial metamerism requires highly dynamic spatiotemporal patterns of activation on the retina. For example, viewing a uniform square of color, which in principle is a constant ratio of L, M, and S activation, actually represents dynamic switching on and off of each cone's activation as it enters and exits the boundary of the square during fixational eye drift. In our color matching experiments, such switches in activation occur on the order of 1000 times per second. In contrast, simply fixing an unchanging activation level at all cones results in the color percept rapidly fading to become invisible – consistent with well-known Troxler fading. The dynamism of the spatiotemporal pattern of activation increases dramatically when considering general image and video percepts, where fine image details move across a cone during eye movement and cause the activation level to fluctuate rapidly at every cone in

the population. Such dynamic spatiotemporal fluctuation in activations occurs continuously in everyday visual perception. Reproducing such patterns in Oz requires fine-grained and complex programmability of the fluctuation in each cell's microdose intensity, and can be thought of as extending computer graphics and virtual reality from screen pixels down to the level of individual photoreceptors.

This class of programmable platform will enable diverse new experiments. For example, Oz can support systematic probing of phenomena such as the threshold at which a small number of cones begin to contribute to a stable color percept [32, 43, 44, 91], or the nonlinear function of a retinal ganglion cell's response to cone activations in its receptive field [92, 93]. Oz can reproduce and then enable programmable "micro-adjustments" to probe the cone activations underlying visual phenomena that operate near the limits of visual perception, such as the two colored-line illusion [94] or visual loss with high levels of cone dropout [95, 96]. More ambitiously, Oz can be programmed to probe the plasticity of human color vision. For example, gene therapy has been used to add a third cone type in adult squirrel monkeys, boosting color dimensionality from 2D to 3D [97]. Analogously, Oz can program signals to the brain as if a subset of cones were filled with a new photopigment type with a different spectral response. Such an approach can flexibly probe neural plasticity to boosting color dimensionality [98] in humans, such as attempting to elicit full trichromatic color vision in a red-green colorblind person, or eliciting tetrachromacy in a human trichromat.

3.4 Methods

Color matching experiments

Color matching tools

In order to characterize the colors seen by subjects when viewing Oz stimuli, we conduct color matching experiments using light sources with known spectral characteristics. We produce Oz stimuli using two stimulation wavelengths: 488 nm, to which all three cone types are sensitive, and 543 nm, which primarily activates L and M cones. Subjects produce matches using two different color matching systems. In one set of experiments, subjects use an DLP Lightcrafter RGB projector as the matching field (Wintech, Carlsbad, CA). We control this display using the Psychophysics Toolbox [72, 73, 74]. In the other experiments, subjects use a tunable-wavelength source with the option of adding additional white light to either the Oz stimulus or matching field using the RGB projector. The tunable-wavelength source is generated using a SuperK supercontinuum laser connected to the SuperL VARIA tunable filter (NKT Photonics, Birkerød, Denmark).

Our custom color matching control panel is a Behringer X-Touch MINI USB Controller (Behringer, Willich, Germany), which we programmed specifically for the color matching task. In experiments using the RGB projector, subjects use 3 free-wheeling dials on this controller to adjust the hue, saturation, and value of the projector-generated matching square, and an additional dial to add desaturating white light to the Oz square if necessary to achieve

an overall match. In experiments using the tunable-wavelength source, subjects use 2 dials to adjust the center wavelength and overall intensity of the matching square, and have the option of using 2 additional dials to add desaturating white light either to the stimulus or the matching field. We use a bandwidth of 10 nm, and the center wavelength can be adjusted over a range from 405 nm to 525 nm.

Subject view

A sketch of the subject's view during color matching is shown in Fig. 3.4. The projector displays a gaze target that we instruct subjects to fixate on for the duration of the experiment. Approximately 4° adjacent to the gaze target, there is a 0.9° square in which both the Oz color and matching color appear in alternation. This geometry ensures that the AOSLO stimulates the classified region of the subject's retina.

The projector generates a gray background field that is 17° in diameter. The chromaticity of this gray background is taken as the reference white point for plotting in Fig. 3.2. The luminance of this gray background is kept at approximately 500 cd/m^2 to establish photopic light levels and avoid interference from rod activation. The gray background pixels are turned off within the Oz/matching square so that no projector light is added to either stimulus. This black square is 1.2x the size of the stimulus, so that any slight misalignment between the AOSLO and projector display does not cause the stimuli to mix with the gray background.

Color matching protocol

During a color matching trial, subjects adjust the controllable color until they achieve a match with the Oz color. The Oz and matching squares of color are spatially coincident and alternate in time, turning on for 1 second each followed by 1 second of darkness in a repeating cycle. Subjects are free to take as much time as necessary to achieve a match. Every 30 seconds, there is a "refresh period" during which the entire field is replaced with a series of multicolored mosaics inspired by the "wipeout" pattern from prior work in hue matching under fixation [90]. Each mosaic appears for 1 second, and each refresh period lasts 15 seconds. In order to submit a match, subjects must have undergone a refresh period within 12 seconds prior and not made any further color adjustments. This is to ensure that the submitted match can be quickly confirmed while the presence of afterimages is minimal.

As an option, subjects can view the Oz and matching squares vertically side-by-side, synchronously alternating 2 seconds on and 2 seconds off. This allows simultaneous comparison of the two colors, but subjects must return to the spatially overlapped and temporally alternating view to judge the match using a common patch of adapted retina before submission.

Subjects may note that the color of the stimulus is not uniform across the entire field of stimulation. In particular, some parts of the field may occasionally appear as the color of the stimulating laser itself, regardless of the LMS activation levels being targeted. This is because any errors in delivery will tend to cause the percept to skew toward the color of the

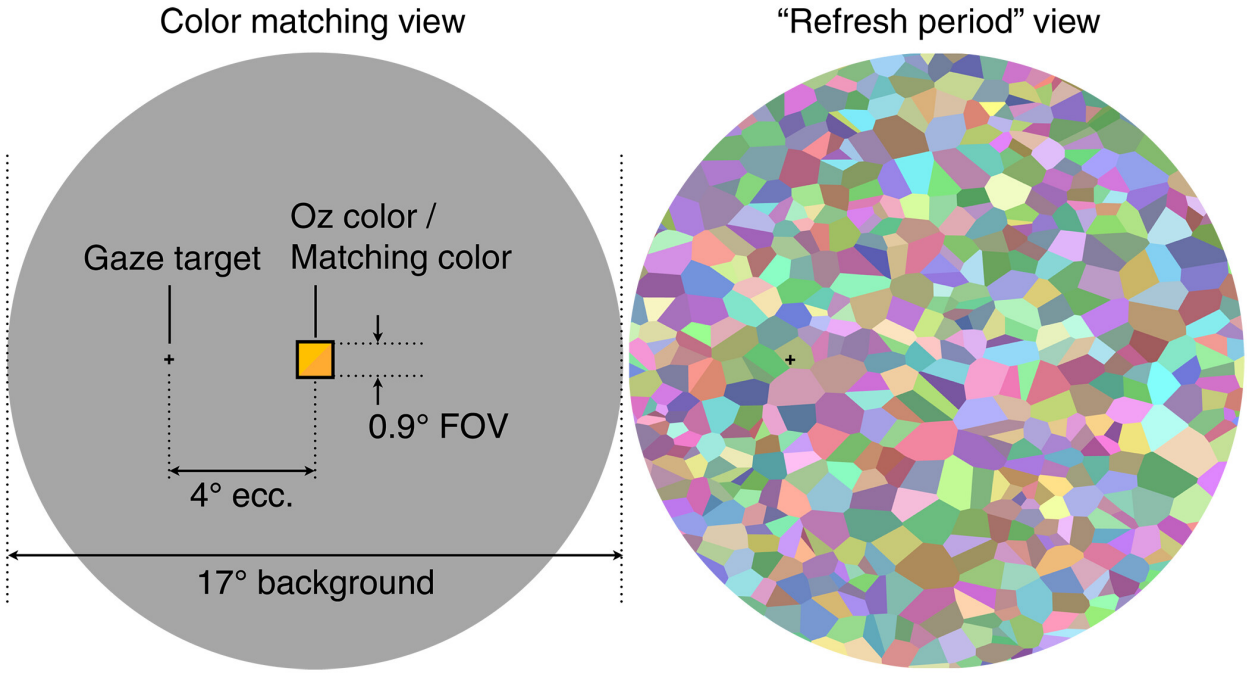

Figure 3.4: **Subject's view during color matching experiment.** Left shows the experimental view. Right shows an example of the multicolored mosaics shown for a periodic 15-second "refresh period".

stimulating laser. Subjects are told to match to the color they see that is most dissimilar from the natural color of the laser.

Plotting color matches

To compute LMS color match coordinates, we spectrally characterize the RGB projector and the tunable laser using a spectroradiometer (PR-650, PhotoResearch (now Jadak), North Syracuse, NY). We measure the spectral power distribution for the projector's red, green, and blue pixel primaries and the linearity of each primary across its 8-bit range, subject to a lookup table which we compute in a calibration step. We compute color match coordinates as the weighted sum of the red, green, and blue primary spectra, each scaled according to the measured output levels corresponding to the matching RGB values selected by the subject. For matches made using the tunable laser system, we individually measure the spectrum of each match setting that was submitted during the experiment. Then, any match involving both the projector's desaturating white and the tunable-wavelength source can be constructed by combining the individually-measured spectra for the two sources.

The projector's gamut is the triangle enclosed by the chromaticity coordinates of its red, green, and blue primaries, as shown in Fig. 3.2a and b. The tunable laser's gamut is the

edge of the spectral locus corresponding to wavelengths between 405 nm and 525 nm. When combined with white light from the projector, its overall gamut for matching is encompassed by the region outlined in Fig. 3.2c. To match colors beyond the boundary of these gamuts, the subject adds an amount of projector white to desaturate the Oz color until a color match is achievable. The resulting coordinates for the Oz color are the coordinates of this desaturating white subtracted from the coordinates of the matching color.

Qualitative hue naming and saturation rating

In addition to color matching, we carry out color *naming* experiments in which subjects observe a stimulus, then name its hue and rate its saturation on a scale from 1 to 4. Subjects see the same fixation cross and gray background, with stimuli appearing at 4° eccentricity from fixation, as in the color matching experiments. Stimuli turn on and off for 2 seconds each on a continuous cycle, and a refresh period occurs before each new stimulus is shown. Subjects are instructed to observe the stimulus for as long as necessary, then to report their qualitative description.

Image and video recognition experiments

In order to quantify our ability to show image and video stimuli in Oz, we conduct 4-alternative forced choice (4AFC) and 2-alternative forced choice (2AFC) image and video recognition tasks. In the image task, we present a line stimulus where the line is oriented in 1 of 4 directions, and the subject is instructed to respond with the direction that they see. The line is delivered using only L-targeted stimulation, and the background is delivered using only M-targeted stimulation. Thus, if the Oz delivery is successful, subjects should be able to use hue information to pass the task. As a control, we deliver the same stimuli but under jittered stimulation, meaning that any hue difference between the foreground and background would be lost, and subjects should not be able to perceive the line.

In the video recognition task, subjecs view a moving dot stimulus and must identify whether it is moving clockwise or counterclockwise. In the same manner as the image task, the dot is presented using L-only stimulation on an M-only background, and jittered trials are included as a control. Thus, the difference in performance between the test and control conditions in these tasks reveals whether our Oz prototype can successfully produce image and video stimuli cone-by-cone.

In these tasks, we aim to eliminate any luminance cues that could allow subjects to detect line orientation or motion direction without using hue information. In particular, because our subjects have more L cones than M cones, a higher density of microdoses are directed at the foreground object than the background in AFC stimuli, which would create a difference in luminance between them. Thus, in a pre-experiment calibration step, subjects adjust the intensity of microdoses directed at the L cones while viewing a jittered moving disk stimulus until the field appears equiluminant. This selected intensity level is then used to render any L-targeted microdoses in the subsequent experiments.

Human subjects

Five subjects were recruited for this experiment [subject number, age, sex, L:M:S ratio]: [10001R, 40, M, 60:32:8], [10003L, 57, M, 58:36:6], [20205R, 44, M, 62:30:8], [20236R, 42, M, 61:30:9], [20253R, 30, F, 62:30:8]. All subjects self-reported as having normal color vision and no ocular disease condition. Subjects 10001R, 10003L, and 20205R are coauthors on the study and were blinded to the test conditions but were aware of the purposes of the study. The other two subjects were members of the participating lab at the University of Washington but were naive to the purposes of the study. The studies were approved by the institutional review boards at the University of California, Berkeley and the University of Washington. We obtained informed consent from all participants.

Prototype system hardware

We built on an AOSLO platform described in previous publications [29, 37]. In this study, we used four spectral channels: a 940 nm channel for wavefront sensing, an 840 nm channel for retinal imaging, a 543 nm channel for retinal stimulation, and a blue channel configurable either as a 488 nm channel for retinal stimulation, or as a wavelength-tunable monochromatic source for matching use. Laser sources of the 940 nm, 840 nm, and 543 nm channels are drawn from the broadband spectral output of a supercontinuum laser (EXR-15, NKT, Birkerød, Denmark). The laser source of the blue channel comes from a separate supercontinuum laser (FIU-15, NKT, Birkerød, Denmark) passed through a tunable filter (VARIA, NKT).

All channels (except the 940 nm channel) are passed through individually fiber-coupled acousto-optic modulators (AOMs) (Brimrose Corporation, Sparks, MD) that can modulate laser intensity up to 50 MHz, and are co-aligned to make the pupil-conjugate planes optically coincident for each channel pair, with respective beam vergence precompensated to be opposite to the longitudinal chromatic aberration (LCA) of a typical human eye [99]. These adjustments ensure that all wavelengths are focused approximately at the same axial retinal depth. At the eye station, the laser powers in all channels are eye-safe, and are measured and recorded before every session.

In experiments, a custom-built Shack-Hartmann wavefront sensor operating with 940 nm light enables adaptive optics correction of eye aberrations in real-time using a deformable mirror (DM97, ALPAO, Montbonnot-Saint-Martin, France), to achieve near-diffraction-limited focus at the photoreceptor layer of the retina, for all wavelength channels. We dilate and cyloplege our subjects using eye drops (1% tropicamide and 2.5% phenylephrine) to enable imaging through the largest possible pupil size (highest numerical aperture) and use adaptive optics to measure and correct for the aberrations of the eye and strive for near-diffraction-limited performance [30].

This laser spot is scanned in a raster pattern over a 0.9° square field-of-view using orthogonally-oriented resonant and galvo mirrors, with a frame resolution of 512×256 and a frame rate of 60 Hz. Light scattered from the retina is descanned and spectrally redirected to

confocal pinholes mounted to individual photomultiplier tubes (PMT) for each wavelength channel.

A custom-built field programmable gate array (FPGA) board (initially in [36]) digitizes and aggregates all PMT signals into 512×16 pixel strips of each frame at 960 Hz as a rolling shutter video stream into a GPU desktop computer that computes cone-by-cone microdose targets. The FPGA receives rasterized 14-bit stimulation signals from the desktop to drive AOMs that modulate the visible-wavelength laser intensities and deliver the intended microdoses of laser light to realtime cone positions.

Additionally, a separate optically co-aligned pathway, similar to the one used in [100], is employed, which incorporates a projector display for showing fixation points and color matching targets, and a pupil camera for real-time pupil tracking.

3.5 Acknowledgments

This chapter was adapted from [48], with co-first authors James Fong and Congli Wang, and co-authors Alexandra E. Boehm, Sofie R. Herbeck, Vimal Prabhu Pandiyan, Brian P. Schmidt, Pavan Tiruveedhula, John E. Vanston, William S. Tuten, Ramkumar Sabesan, Austin Roorda, and Ren Ng. James Fong was responsible for developing theory and modeling of the colors perceived in Oz, plotting color matching results in color space, and developing the Wizard software for controlling the cone-targeted stimulation. I was responsible for designing the color matching and image and video recognition experiments, implementing the experiment control code, and conducting the psychophysical experiments. This work was supported by a Hellman Fellowship, FHL Vive Center Seed Grant, Air Force Office of Scientific Research grant FA9550-20-1-0195, Air Force Office of Scientific Research grant FA9550-21-1-0230, National Institutes of Health grant R01EY023591, National Institutes of Health grant R01EY029710, National Institutes of Health grant U01EY032055, and a Burroughs Wellcome Fund Career Award at the Scientific Interface.

Chapter 4

Revealing the Benefit of Eye Motion for Acuity under Emulated Cone Loss

Retinal degenerative diseases progressively erode the cone photoreceptor mosaic, reducing the retina's spatial sampling power, yet visual acuity is remarkably resilient to cone loss. Prior work has shown that clinically normal visual acuity (20/25 or better) can persist despite up to 50% of cone cells being lost [96, 101]. However, studies on individuals with retinal degeneration are limited by patient recruitment and cannot control for patients' stage of disease progression, creating the need for an experimental paradigm that can mimic these diseases in healthy subjects. The Oz Vision system creates visual percepts through programmable, per-cell stimulation of thousands of cone cells. We reprogram this system to emulate cone loss in healthy eyes by withholding stimulation from a subset of randomly-selected cones, rendering them inactive, in a method we term "cone dropout." Using this approach, we characterize the visual system's robustness to cone loss, showing that visual acuity declines nonlinearly with increasing cone dropout. Importantly, we uncover the compensatory benefit that eye motion provides under cone-deprived conditions, finding that at the highest level of dropout, a visual system with eye motion has an equivalent acuity to a static dropout condition with nearly twice as many sampling elements. Through analysis of eye motion and stimulation data, we find that this benefit arises from the additional information accumulated by "surviving" cones as they sample more of the letter through fixational eye motion.

4.1 Introduction

Retinal degenerative diseases degrade vision by causing photoreceptor death and loss over time [102]. Despite this reduction in spatial sampling elements, visual acuity is remarkably robust to cone loss. In patients with retinitis pigmentosa, clinically normal acuity levels ($\geq$20/25) are maintained with up to a 50% reduction in cone density relative to the average [96, 101]. However, study of visual function under retinal degeneration is limited by the

recruitment of patients with the diseases in question. It is further complicated by the fact that patients may be at different stages of progression in those diseases, the functional status of remaining cones is unknown, and that factors beyond photoreceptor degeneration may contribute to vision loss [103, 104]. Thus, the mechanism underlying the preservation of acuity under cone loss has not been fully characterized.

In light of the challenges posed by patient recruitment, prior work has attempted to simulate cone loss in healthy subjects. This has historically been achieved through randomly blanking pixels on a display and measuring the impact on subject performance in tasks such as letter identification [105, 106], grating identification [95, 106], and reading [107]. These implementations did not exactly reproduce the conditions of retinal degeneration, though, as the sampling loss was not fixed to the retina as the eye moved and was instead fixed to stimuli in the world. Other studies simulating visual impairment in healthy subjects have accounted for this consideration by stabilizing artificial scotomas to the retina using eye tracking [108, 109, 110, 111] and more recently using extended reality technologies in head-mounted displays [112, 113, 114, 115]. However, these approaches were limited in spatial precision due to tracking error [116] and latency between tracking and stimulus updates ranging from 10-80 ms. As a result, the artificial scotomas used in those studies typically spanned multiple degrees of visual angle such that these errors were small by comparison, and thus could not reliably mimic diseases that cause degradation at the much smaller single-cone level.

The Oz Vision system recreates visual percepts on a per-cone basis through optical stimulation of individual cone photoreceptors at population scales. We implement this principle using an Adaptive Optic Scanning Light Ophthalmoscope (AOSLO), which images the retina, tracks the eye's motion with sub-cone precision, and stimulates individual cones with 4-ms latency [48]. This technology has previously been used to target cones based on their spectral type as described in Chapter 3, but here we programmatically adapt it to exclude a subset of *all* cones from the stimulation pattern irrespective of their type. That is, we use the system to deliver stimuli cone-by-cone, but delete a subset of randomly-selected cones from an underlying retina map in software such that these cones do not receive stimulation and are rendered effectively "dead." Then, as the subject moves their eye across the stimulus, only the "surviving" cones are stimulated as they pass under the world-fixed stimulus, and the pattern of "dead" cones remains fixed to their retina. In this way, we can use this system to emulate cone loss that moves *with* the eye, recreating the conditions of retinal degeneration more accurately and on a finer scale than previously possible. This stimulation platform provides the opportunity to emulate cone loss in any subject and systematically characterize its effect on visual function.

With this technology, we find that vision is adversely affected by cone loss, but that eye motion acts as a compensatory mechanism that preserves visual acuity under a degraded cone mosaic. It has been shown previously that in subjects with normal vision, eye motion can enhance visual acuity [26, 23, 24]. A model developed to explain this phenomenon also predicted that eye motion would provide a benefit for reconstructing a letter E stimulus under conditions of cone loss [117]. However, no study has measured the effect of eye motion

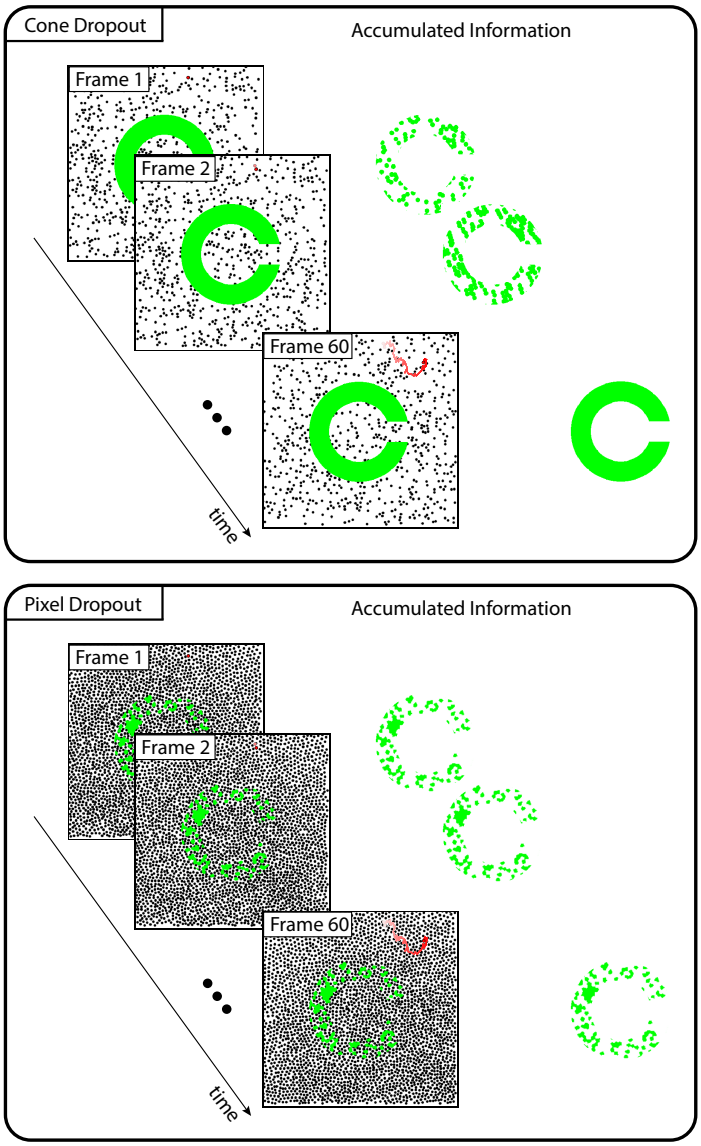

Figure 4.1: **Dropout conditions.** The two panels compare the cone and pixel dropout conditions with 75% dropout. The frames on the left show the retinal mosaic with cones in black and the green C stimulus overlaid. Due to fixational eye motion, the retinal mosaic moves relative to the world-fixed C stimulus between each frame. The eye motion trajectory is shown as a red trace overlaid on the frame, with lighter colors indicating time points further in the past. In the cone dropout condition (top), a fully intact stimulus is sampled by a retinal mosaic where a percentage of the cones have been removed randomly. In the pixel dropout condition (bottom), a percentage of pixels are removed randomly from the stimulus, which is sampled by an intact retinal mosaic. The right shows the accumulation of information in each case. Under fixational eye motion, the loss moves with the eye in the cone dropout condition, allowing for the intact parts of the mosaic to sample more of the letter, building a more filled-in percept over time. In the pixel dropout condition, the loss remains fixed to the stimulus and no information is accumulated through eye motion.

on visual acuity with cone loss in real subjects. We fill this gap by conducting experiments where we programmatically vary the degree of cone loss and measure its impact on visual acuity in a Landolt C task, where subjects must judge the orientation of C stimuli of varying sizes. We compare performance under the condition of emulated cone loss to one where loss is fixed to the stimulus rather than the retina, thereby revealing the role of eye motion in accumulating information when sampling with a degenerated retinal mosaic.

4.2 Results

Subjects performed a Landolt C visual acuity task under two conditions of sampling loss: a "cone dropout" condition, where cones were removed from the retina map, and a "pixel dropout" condition, where pixels were removed from the stimulus itself (see Figure 4.1). In the cone dropout condition, the sampling loss is fixed to the retina and moves with it as the eye moves. In the pixel dropout condition, the loss is fixed to the Landolt C stimulus and does not change over time. The comparison of performance between these two conditions offers insight into the role of eye motion because the percentage of sampling loss present in the stimulus delivered to the retina would be approximately equivalent across the two conditions at any given moment. However, in the cone dropout condition, as the eye moves with fixational eye motion, the visual system would receive information about different regions of the letter C as the intact parts of the retinal mosaic sampled them. Thus, if the visual system makes use of information accumulated over time through eye motion, this would confer a benefit in acuity in the cone dropout condition over the pixel dropout condition.

Acuity threshold experiment

In the first experiment, we measured acuity thresholds using a Landolt C 4-alternative forced choice (4AFC) task. Landolt C stimuli were presented for 1 second, and subjects responded with the orientation of the letter that they perceived (up, down, left, or right). Using randomly-interleaved QUEST staircase procedures to vary the letter size [118], we determined acuity thresholds under 11 total conditions: 5 percentages of cone dropout, 5 equivalent percentages of pixel dropout, and one no-dropout condition. Each step in these 5 dropout percentages corresponded to reducing the total number of cones or pixels by half.

The results are shown in Figure 4.2. We plot the measured acuity thresholds for 4 subjects as a function of the fraction of cones remaining in the mosaic and the equivalent percentages of dropout for the cone and pixel dropout conditions. We show the average acuity across all subjects at each percentage tested, and fit linear models to these averages and to each individual subject's data. Taken as a whole, our data indicates that the cone dropout condition does confer an acuity advantage over the pixel dropout condition spanning approximately one or more rows on a standard acuity chart.

First, we find that visual acuity in logMAR worsens logarithmically as the dropout percentage increases for the 4 subjects tested ($R^2 = 0.945$ for cone dropout and $R^2 = 0.953$ for pixel dropout). This trend is conveyed through linear fits on the log-log plot. The nonlinear relationship between dropout and acuity that we find under emulated cone loss is consistent with prior studies done with real patients, thereby confirming that visual acuity is well-preserved up to 50% cone loss [96, 101]. We use analysis of covariance (ANCOVA) to test for the effects of dropout percentage, dropout type, and the interaction between the two. When looking at the data across all subjects, we find a significant relationship between acuity and dropout percentage ($p = 3.8 \times 10^{-30}$). There is also a significant difference between acuity on average between the pixel and cone dropout conditions ($p = 0.00014$). Most importantly, the slope of the relationship between acuity and dropout percentage is significantly different between the pixel and cone dropout conditions ($p = 0.027$). That is, eye motion appears to benefit visual acuity when cones are lost from the retinal mosaic.

To contextualize the benefit in acuity provided by eye motion, we indicate the acuity levels corresponding to rows on a standard eye chart on the right side of Figure 4.2. We can see that at dropout levels of 75% and above, the improvement in acuity from the cone dropout over the pixel dropout condition spans approximately one row or more on the acuity chart. Another feature of the data is that, as dropout increases, the average acuity threshold at a given percentage of cone dropout gets closer to the average acuity threshold at the preceding percentage of pixel dropout. In particular, at the highest level of dropout, the presence of eye motion under cone dropout can effectively recover the acuity level at a pixel dropout condition that has nearly twice as many sampling elements.

Stimulus duration experiment

In a second experiment, we varied the duration of the Landolt C stimulus and measured subject performance for the orientation task under the cone and pixel dropout conditions. We tested 7 durations, spaced logarithmically between 66.7 ms and 4.27 s. The two conditions and 7 durations were randomly interleaved. We kept the dropout percentage fixed at 93.75%, chosen so that the task would be challenging enough to reveal differences in performance across durations and conditions. The letter size was chosen based on each subject's previously-measured acuity threshold at 93.75% dropout and kept fixed for the entire experiment (see Methods for details).

Figure 4.3 shows the results of the experiment varying stimulus duration. We plot Δ Performance versus the stimulus duration, where Δ Performance is the difference in fraction correct between the cone and pixel dropout conditions. This means that points above zero correspond to instances where subjects performed better under the cone dropout condition, whereas points below zero indicate where subjects performed better under the pixel dropout condition. We see that at shorter durations, points are closer to zero, meaning that subjects perform similarly under the pixel and cone dropout conditions. At longer durations, subjects tend toward performing better under the cone dropout condition than in the pixel dropout condition, with the point at the longest duration of 4.27 s being significant (p = 0.018).

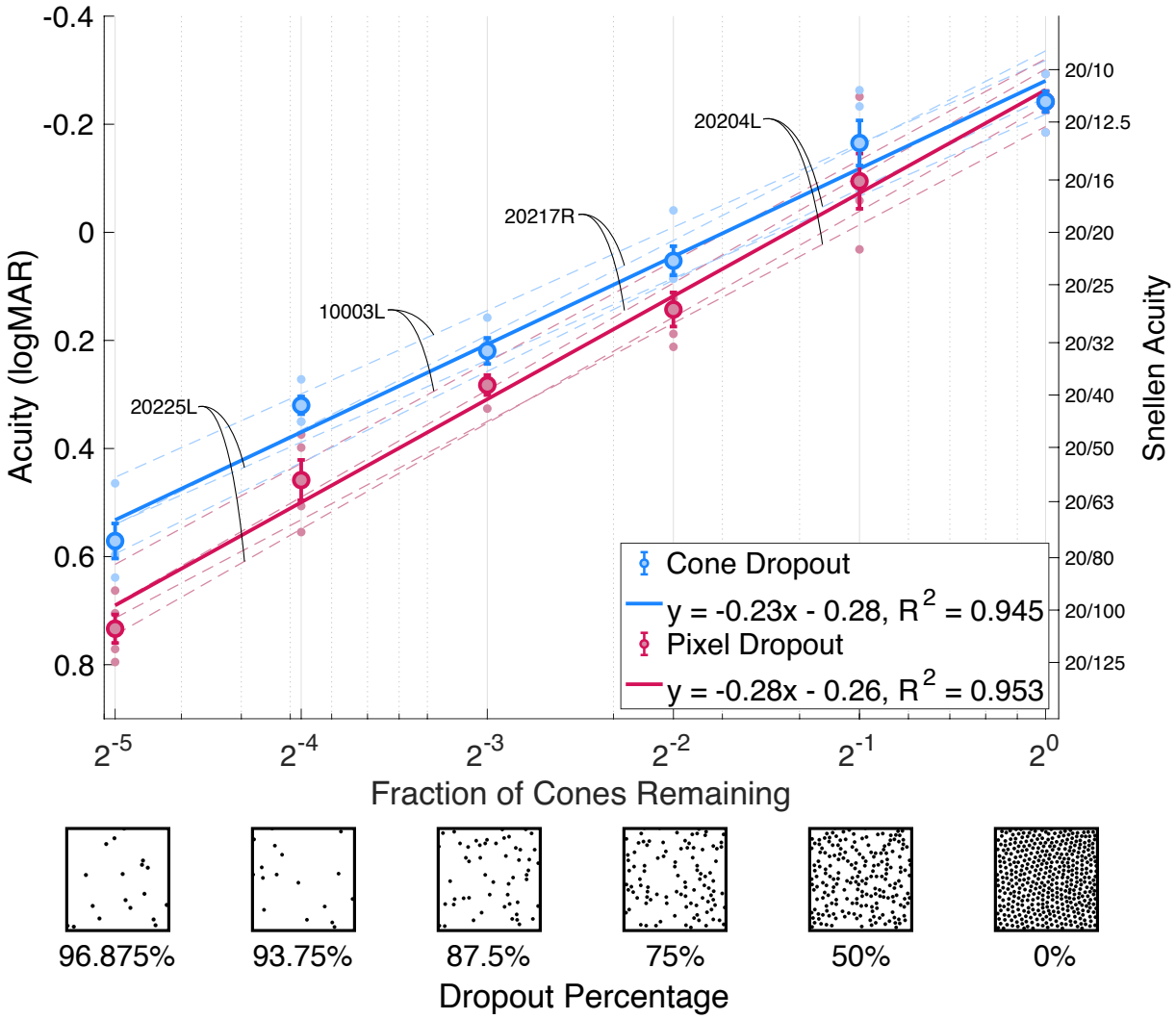

Figure 4.2: **Acuity threshold experiment.** Acuity is plotted versus the fraction of cones remaining and the equivalent dropout percentage under the cone dropout condition (blue) and the pixel dropout condition (red) for 4 subjects. Dashed lines show the fitted regression lines to individual subject data, while the solid lines show the fitted regression line across all 4 subjects for the 2 conditions, where y is the logMAR acuity and x is the logarithm of the fraction of cones remaining in the mosaic. The bold points show the average acuity across subjects with error bars indicating the standard error of the mean.

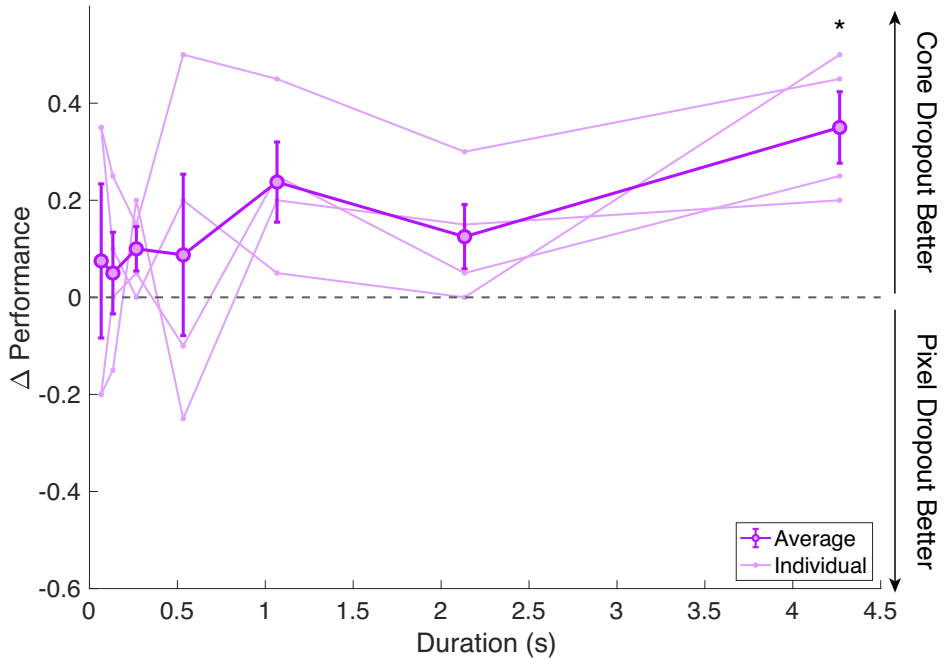

Figure 4.3: **Stimulus duration experiment.** The difference in fraction correct between the cone and pixel dropout conditions on a 4AFC Landolt C task is plotted versus stimulus duration. Individual subject Δ Performance is plotted with faint lines. The average Δ Performance across those 4 subjects is plotted with dark lines and error bars indicating the standard error of the mean.

These results provide further insight into the importance of eye motion for recovering information under cone-deprived conditions. At short durations, it makes sense that the two conditions would result in similar performance, as there has been little time for the eye to move and sample new parts of the stimulus under the cone dropout condition. This psychophysical result therefore additionally serves as an experimental validation that the two conditions are perceptually equivalent at a single-frame level. For longer durations, under the pixel dropout condition, no new information could be gained about the stimulus over time. However, the benefit from eye motion in the cone dropout condition was revealed by the performance improvement as stimulus duration increased, as the eye had more time to move an appreciable amount relative to the size of the stimulus.

Analysis of recorded trial data

In the system we use for cone-by-cone stimulation, a rich stream of data is recorded with every trial, including a video of the moving retina, a record of the eye motion as it was

tracked in real time, and a log of all delivered microdoses of light with their corresponding retinal locations. Using this recorded data, we can reconstruct the stimulation pattern that the subject received on any given trial, and conduct analyses in order to help explain our psychophysical results.

Sampling coverage analysis

In the psychophysical experiments measuring acuity thresholds as a function of dropout percentage, subjects showed better acuity under the cone dropout condition as compared to the pixel dropout condition as dropout increased. The intuitive explanation for such a difference is that under the cone dropout condition, eye motion causes more parts of the letter to be sampled by intact parts of the retinal mosaic, which allows for the visual system to take in more information about the letter, leading to a more accurate judgment of letter orientation. This difference in accumulated information between cone and pixel dropout is depicted visually in Figure 4.1. Using the actual recorded stimulation data, we can examine whether this intuitive understanding is supported by the recorded doses of light that were received by the visual system under the two conditions.

In order to examine the advantage provided by eye motion in the cone dropout condition, we perform an analysis computing the sampling coverage of the Landolt C stimulus on every trial in the experiments measuring acuity thresholds. We define the sampling coverage as the percentage of the letter's area that was sampled by a cone at any point during a trial (see Methods for more details on the sampling coverage calculation).

We process every trial delivered during the acuity threshold experiment for all 4 subjects at each dropout percentage under the cone and pixel dropout conditions. We then compute the average sampling coverage across all trials under a given dropout percentage for the two conditions. The results of the analysis are shown in Figure 4.4a, showing the average sampling coverage versus the fraction of cones remaining. The dashed lines show the fit to each individual subject's data while the solid lines show the fit across all subjects.

We see that the trends in this analysis agree well with the psychophysical results in Figure 4.2. First, as would be predicted, we see that the sampling coverage is higher under the cone dropout condition (cyan) than under the pixel dropout condition (orange). Additionally, both sets of data are fit well by a logarithmic relationship ($R^2 = 0.945$ and 0.953 for the psychophysical data and $R^2 = 0.97$ and 0.972 for the sampling coverage analysis). Qualitatively, the slopes of these best-fit lines appear similar between Figure 4.2 and Figure 4.4a. That is, the best-fit line for the pixel dropout condition is steeper than the best-fit line for the cone dropout condition in both cases. These similarities suggest that the quantity sampling coverage, which is calculated directly from stimulation data, can be used as an explanatory metric for the acuities measured during the acuity threshold experiments.

To examine the sampling coverage as an explanatory metric more directly, we plot the measured acuity for each subject under each dropout condition against the corresponding calculated sampling coverage in Figure 4.4b. We find that the resulting data from both the cone and pixel dropout conditions can be fit well by a single linear relationship (R^2

= 0.929). Importantly, plotting the data in this way causes the acuity gap between cone and pixel dropout to disappear. That is, the difference in measured acuity between the two conditions is captured completely by the difference in sampling coverage. This in turn reflects the key benefit provided by eye motion under the cone dropout condition, where the visual system is able to sample a larger fraction of the occluded Landolt C stimulus.

In this analysis, we sum all microdoses delivered over the course of each 1-second trial, in essence assuming that the temporal integration period of the visual system is infinite. As shown in the experiment varying stimulus duration (see Figure 4.3), subject performance does seem to improve up to 1 second, after which performance plateaus. Thus, under our experimental conditions, it does seem that the visual system can synthesize all of the additional information gathered over of the course of the 1-second trial. However, in practice, we would not expect for the sampling coverage to continue improving indefinitely with increasing stimulus durations. That is, analysis done for experiments with longer trials should include a finite temporal integration window when computing the sampling coverage.

Analysis of eye motion data

The consistent performance gap between the cone and pixel dropout conditions seen in our psychophysical results suggest that eye motion is used to benefit acuity under cone-deprived conditions. Prior work has found changes in eye movement patterns in response to simulated scotomas [119, 120] and in patients with retinal degeneration [121, 122]. Thus, we explored the possibility that similar changes could be present in the eye motion traces that were recorded during each experiment.

To determine whether subjects adopted specific gaze strategies in response to the dropout conditions, we examined both the overall magnitude of their eye motion as well as its directional characteristics. To examine the magnitude quantitatively, we computed the iso-density contour areas (ISOAs) containing 68% of the eye motion data from the duration experiment for each subject and dropout condition (see Methods). Using a two-sample t-test, we found no significant difference in the ISOAs between cone and pixel dropout for all 4 subjects, indicating that subjects did not move their eye any more or less under the cone dropout condition as compared to the pixel dropout condition.

We explore whether directional biases arise in subjects' eye motion traces using analysis inspired by [26], rotating each eye motion trace as necessary such that all traces are aligned to the veridical orientation of the Landolt C. This aims to reveal whether subjects fixational eye movements tend toward finding the gap in the letter, which they would expect to find at 1 of its 4 possible locations. However, again, we found no evidence of directional differences between dropout conditions or with increasing stimulus duration.

In our analysis of the recorded eye motion traces, we found no clear trends in overall magnitude or directional characteristics, suggesting that the visual system can build a filled-in percept passively through unbiased fixational eye motion. However, it should be noted that in these experiments, the dropout conditions were presented in a random order, meaning that the form of dropout could change between cone and pixel dropout from trial to trial.

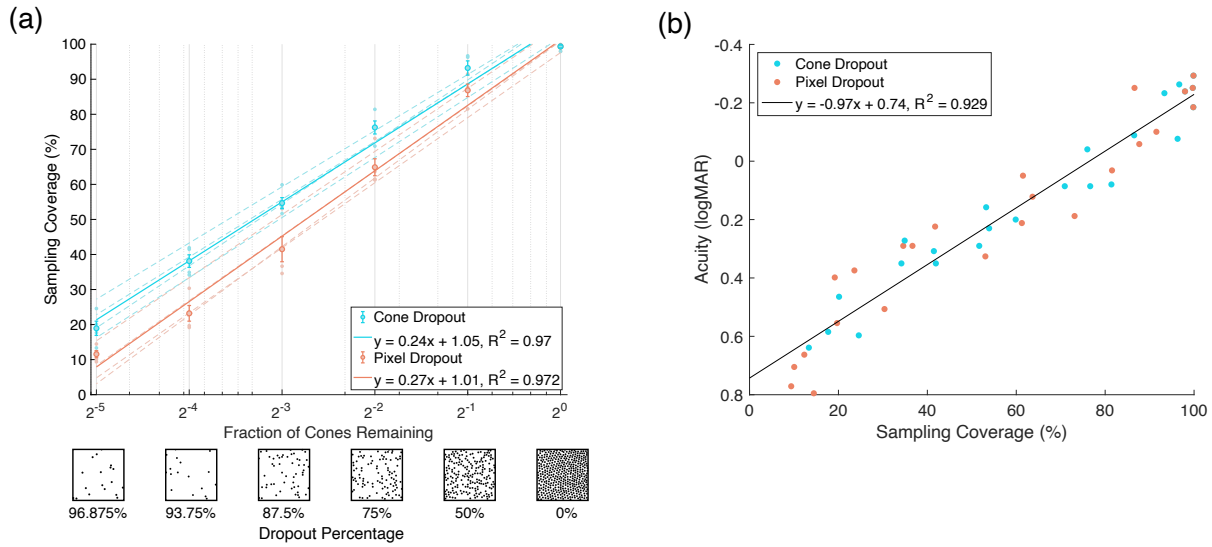

Figure 4.4: **Sampling coverage analysis.** (a) The average sampling coverage of the Landolt C stimulus across all trials in the acuity threshold experiment is plotted versus the fraction of cones remaining and the equivalent dropout percentage for the cone dropout condition (cyan) and the pixel dropout condition (orange). The dashed lines show the fits to each individual subject's data, and the solid lines show the fits to the data averaged across subjects, where y is the sampling coverage in decimal form and x is the logarithm of the fraction of cones remaining in the mosaic. (b) The measured acuity for each subject at each dropout percentage is plotted versus the calculated sampling coverage from the corresponding trials. Each point represents one subject at one dropout percentage, either under the cone dropout (cyan) or pixel dropout (orange) condition. The data is fit by a linear relationship (black), where y is the logMAR acuity and x is the sampling coverage in decimal form.

Thus, it remains to be seen whether a subject would adopt strategic eye motion behavior in response to a fixed pattern of cone dropout that persisted for a longer period of time.

4.3 Discussion

We have developed a technology for faithfully recreating the conditions of cone loss in healthy subjects, and we use it to characterize the relationship between the degree of cone loss and visual acuity. This experimental paradigm solves a set of challenges faced by prior work studying patients with retinal degeneration. Those studies first needed to specifically recruit patients with the diseases of interest. They could not control for the stage of disease progression in each of these patients, and thus were forced to compare patients with a wide

range of severity in cone loss. Image-based metrics such as cone spacing may not have been sufficient to know the true degree of cone loss in each patient, as baseline cone density can vary between individuals [123], and even cones that appear dark in a retinal image may still be functional [124, 125]. We, however, have complete control over the emulated percentage of cone loss in each of our subjects and can therefore study its effects freely without facing such challenges.

Others have tried to address those challenges by simulating cone loss through randomly blanking pixels in stimuli on a monitor [106, 95, 106, 107]. One such study even attempted to simulate motion by shifting the blanked pixels midway through the presentation, but lacked the technical capability for stabilization [105]. Thus, these implementations did not capture the fact that real cone loss is fixed to the retina and will move with the retina due to eye motion. In fact, we have shown that there is indeed a difference in performance between a condition where pixels are removed from the stimulus itself and a condition where cones are removed from the mosaic. That is, using those prior studies as a benchmark would likely lead to an *underestimation* of the degree of cone loss based on a subject's measured acuity, as those results did not account for the benefit in performance due to eye motion. Therefore, it is critical to consider the impact of eye motion when studying visual function under cone loss.

Our experiments revealed a nonlinear relationship between acuity and the degree of emulated cone loss which resembled the trends found in work with real patients [96, 101]. In particular, our results suggest that one can lose 50% of their cones while maintaining acuity levels of 20/20 or better. This has implications for technologies that aim to restore vision through the use of light-sensitive retinal implants [126, 127]. Such technologies consist of a photovoltaic array with an effective sampling density that is much lower than that of a healthy retinal mosaic. The cone dropout condition mimics this loss in sampling power, and thus the acuity levels that we measure can serve as useful benchmarks for the spatial frequency of the array that is required to achieve a target acuity.

In addition to its capability to emulate the conditions of cone loss, our system also captures a stream of data with every trial that can be used to better interpret our psychophysical results. Using this recorded data, we examine both the recorded stimulation patterns and eye motion traces in order to draw conclusions about how acuity improves under the cone dropout condition. We are able to compute what percentage of the Landolt C stimulus was sampled on every trial, and find that this metric best explains the trends in acuity as impacted by dropout condition and percentage. That is, the psychophysical results can be well-predicted directly from the stimulation patterns recorded during each trial.

These experiments mark the first usage of the Oz system for emulating cone loss. In the present study, we apply this technology to characterize visual acuity specifically. However, retinal degeneration has been shown to degrade vision on other metrics such as motion detection [128, 129], small-spot detection [130, 131], and contrast sensitivity [132, 133]. In our system, we can freely vary the experimental task and stimulus conditions to study these aspects of visual function in future work. This technology additionally opens up possibilities for emulating retinal diseases with different forms of dropout. Here, we implement dropout

on a cone-by-cone basis, but in general, we have the programmability to fix any pattern of loss to the retina. Future studies could implement intermediate levels of cone degradation rather than binary cone loss, larger spatial scales of dropout, or dropout with varying degrees of spatial uniformity. Thus, this platform enables general study of the way spatial sampling loss impacts visual performance, presenting the opportunity to better understand the implications of a wide range of diseases affecting the retina.

4.4 Methods

Subjects

Four experienced male subjects (ages 23-58) were recruited for these experiments, two of whom are authors on this study. All subjects provided informed consent before participating in the experiments. This study was approved by the Institutional Review Board at the University of California, Berkeley.

Adaptive optics scanning light ophthalmoscopy

All experiments were run using an AOSLO that simultaneously images and stimulates the retina, while correcting for the imperfect optics of the eye. The adaptive optics component consists of a Shack-Hartmann wavefront sensor which measures the aberrations of the eye, operating in closed loop with a deformable mirror which changes its shape in order to counteract those aberrations. The scanning component of the system consists of two scanners conjugate to the pupil plane, with one resonant scanner operating at 16 kHz in the horizontal dimension and another galvanometric scanner operating at 60 Hz in the vertical dimension. Combined, they scan the outgoing beam of laser light across the retina over a 0.9°-field at a frame rate of 60 Hz, and relay the reflected light back through the system in order to produce a retinal image. The reflected light is detected using photomultiplier tubes.

The AOSLO contains several wavelength channels; in this experiment, we use three of them. Wavefront sensing for the adaptive optics correction was done at 940 nm, retinal imaging was done at 840 nm, and visual stimulation was done at 543 nm.

Cone-by-cone stimulation

In order to deliver cone-by-cone stimulation, we use custom software called Wizard. This software tracks the eye's motion by breaking the incoming infrared retinal image into strips and locating each strip against a pre-loaded map of the subject's fovea (more details in *Eye Motion Analysis* section) [34, 48]. This map contains metadata that labels the locations of all of the cones within the stimulated region. For the four subjects in this study, the total number of cones in these maps ranged from 17,407 to 26,322. Using these cone locations, Wizard then communicates with an acousto-optic modulator (AOM) to modulate the visible-

wavelength channel as it scans across the retina such that it turns on only when it passes over the intended target cones. The latency between the strip used for tracking and the strip where stimulation is delivered in response to that tracking information is approximately 4 ms.

Stimulus preparation

Cone dropout condition

In order to implement the cone dropout condition, a randomly-selected subset of the cone labels were removed from the retina map in a proportion equaling the desired dropout percentage. Thus, when the system intended to deliver a C stimulus to the fovea, it would exclude a percentage of the cones from its stimulation as specified by the pre-loaded map.

Pixel dropout condition

In the pixel dropout condition, we remove pixels from the Landolt C stimulus image. Rather than removing pixels completely randomly, we took measures so that the spatial distribution of the pixel removal would match the spatial characteristics of the cone dropout condition. First, we create a Voronoi tessellation of the subject's foveal cone map. Next, we randomly select a percentage of the Voronoi cells and create a binary mask, where these chosen cells are set to 0 and the rest are set to 1. We then apply this binary mask to the C stimulus. These stimuli are then delivered through our custom stimulation software, sampled by a retina map containing no dropout. As a result, the pixel dropout stimulus is approximately equivalent to the cone dropout stimulus at any given instant, both in an overall radiometric sense and in terms of its spatial characteristics. This was validated psychophysically by the similarity in performance between the two conditions at short stimulus durations (see Figure 4.3). The operative difference between the two is that the information loss is fixed to the stimulus in the pixel dropout case, and fixed to the retina in the cone dropout case, which becomes perceptually important as stimulus duration increases.

Experimental protocol

Experiment setup

Prior to each experiment, we dilate and cycloplege subjects using drops of 1.0% tropicamide and 2.5% phenylephrine hydrochloride. Subjects are stabilized in the system using a bite bar and moved into alignment using translational stages. For each subject, we determine the best defocus setting for visible stimulation by collecting a series of through-focus images at 543 nm. During each experimental session, we capture a sequence of 0.9° videos in 840 nm to produce a 1.8° × 1.8° map of the fovea which is used for tracking [47]. We additionally measure and correct for the transverse chromatic aberration between our imaging and stimulating wavelengths using the method described in [48].

Acuity threshold experiment

In the acuity threshold experiment, subjects performed a Landolt C 4AFC orientation identification task. We measured acuity under 5 percentages of cone dropout and 5 equivalent percentages of pixel dropout, along with one no-dropout condition, for a total of 11 conditions. The 5 dropout percentages were logarithmically spaced as follows: 50%, 75%, 87.5%, 93.75%, and 96.875%.

For each condition, we ran 4 interleaved QUEST staircase procedures [118] with 20 trials per staircase. We ran equivalent percentages of cone and pixel dropout together, with their staircases randomly interleaved in a block of trials. The no-dropout condition was randomly interleaved with the 50% cone and pixel dropout conditions.

On a given trial, a beep preceded the stimulus, then the stimulus was presented for 1 second, followed by another beep indicating that the subject should respond with their perceived orientation. Another sound played after the subject's response, and the next trial would begin immediately.

Stimulus duration experiment

The task in the stimulus duration experiment was the same Landolt C 4AFC task as in the acuity threshold experiment. We tested 7 durations which were logarithmically spaced as follows: 66.7 ms, 133.3 ms, 266.7 ms, 533.3 ms, 1.07 s, 2.13 s, and 4.27 s. These durations correspond to integer multiples of 16.7 ms, the duration of one frame in our 60-Hz frame rate system. Each duration was shown under both the cone and pixel dropout conditions, with 20 trials per duration-dropout combination. All conditions and durations were randomly interleaved.

As in the acuity threshold experiment, a beep preceded the stimulus, then the stimulus was shown for a duration chosen from one of the 7 options, followed by another beep which prompted the subject to a respond. A sound played when the subject's response was received and the next trial would begin immediately.

In this experiment, we kept the letter size and dropout percentage fixed, and varied only the stimulus duration. We chose the dropout percentage to be 93.75%, so that the dropout was extreme enough to avoid ceiling effects in performance. In order to choose the letter size, we took into consideration all of the data gathered across subjects in the acuity threshold experiment. We normalized each subject's data to align their psychometric functions by the threshold letter sizes under the cone dropout condition. Then, we fit a single psychometric function to all cone dropout data and to all pixel dropout data separately. We found that the difference in performance between the two conditions was maximized at a 16% larger letter than the threshold. That is, we chose the letter size in the duration experiment to be 16% larger than each individual subject's previously-determined acuity threshold letter size for the 93.75% dropout condition.

Eye motion analysis

Each trial presented during the experiments has an associated set of data saved along with it. This includes a log of all microdoses that were delivered, the retina map used for tracking, as well as a record of the eye's motion during the trial.

In the Oz Vision system, each incoming infrared image is broken into 16 strips, which each consist of 16 by 512 pixels. Each strip is located against the premade retina map to produce a record of the eye's position. There are 16 strips per incoming frame, and our system operates at a frame rate of 60 Hz, resulting in an eye motion trace with a sampling frequency of 960 Hz.

To perform analysis of the eye motion data, we use MATLAB (MathWorks, Natick, MA, USA). With custom software, we iterate through all eye motion data files and extract the x- and y- locations with their associated timepoints. If there are any samples missing due to tracking failures, the missing points are interpolated between the two most recent tracked locations such that there is position data at every timepoint.

With the saved eye motion data, we aggregated all eye motion traces collected during the stimulus duration experiment and separated them by subject and by dropout condition. For each set of eye motion data, we aligned all traces at the centroid of each of their individual distributions. We then computed the iso-density contour that contained 68% of the eye motion data in these aggregated traces, and calculated the area enclosed by that contour.

Sampling coverage analysis

To compute the sampling coverage for a given trial, we first find the locations of each microdose of light delivered during a given trial. This information is saved in a .csv file with every recorded trial. We create a 2D binary matrix containing a map of each of the pixels where a microdose was delivered. Then, we convolve this map of microdose locations with a 2D Gaussian kernel with $\sigma = 0.1$ arcmin, in order to simulate the effect of the system point spread function (PSF) which blurs each microdose of light that is delivered to the retina. We binarize the result of this convolution to create a map of all pixels that were sampled over the course of the trial. Finally, we mask this pixel map with a Landolt C with size and orientation corresponding to the current trial, and compute the percentage of pixels covered by the stimulation pattern out of the total possible area contained in the letter. This provides a measure of the sampling coverage of the letter by the subject on each trial.

4.5 Appendix

Cone dropout adaptation experiments

In experiments studying visual acuity under cone dropout, we did not perform a formal measurement of subjects' qualitative experiences. However, in viewing stimuli with dropout, subjects reported that the initial speckle resulting from the missing cones seemed to fill in

over time, despite no change being made to the stimulus itself. This indicated that some temporal adaptation may have been occurring, which warranted further investigation. To that end, we conducted preliminary experiments which sought to measure this qualitative observation more rigorously.

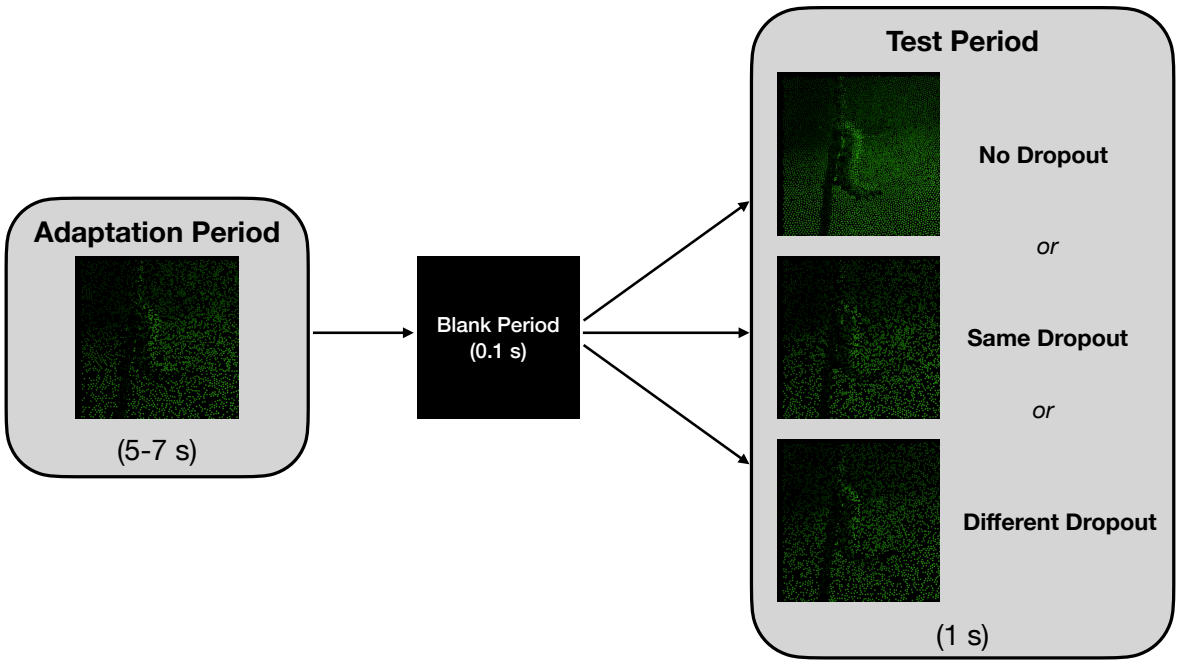

Figure 4.5: **Cone dropout adaptation experiment design.** The schematic diagram depicts the design of a single trial in the adaptation experiment. First, subjects view a stimulus subject to a specific pattern of cone dropout for 5-7 seconds. Then, following a brief blank period, subjects see a test stimulus with either no dropout, the same dropout pattern, or a different spatial pattern of dropout with the same overall percentage. The subject then rates the uniformity of the second stimulus shown.

The first experiment's design is shown in Figure 4.5. Each trial in this experiment begins with an adaptation period ranging from 5-7 seconds. During this period, a 50% cone dropout pattern is fixed to the subject's retina as they view an image stimulus. A blank period of 0.1 seconds follows the adaptation period in order to mask the transition to the subsequent test period. In the test period, a stimulus belonging to one of three categories is shown. In one case, the original stimulus image is shown with no dropout applied. In another case, the image is shown with the same dropout map as was used in the adaptation period. In the third case, the same percentage of dropout is applied, but the spatial pattern of the dropout is different than in the adaptation period.

Following each trial, the subject's task is to rate the uniformity of the test stimulus on a scale from 1 to 4, with 4 corresponding to a judgment of 'perfectly uniform.' The non-dropout case serves as a control which subjects would be expected to rate a 4 on the uniformity scale. In isolation, the two dropout conditions should appear to have the same level of uniformity, as they are both subject to the same overall percentage of dropout. However, if adaptation were to take place during the adaptation period, one would expect to see that subjects rate the same-dropout condition as more uniform than the different-dropout condition on average. Thus, the comparison of ratings between these two dropout conditions offers insight into whether adaptation is taking place.

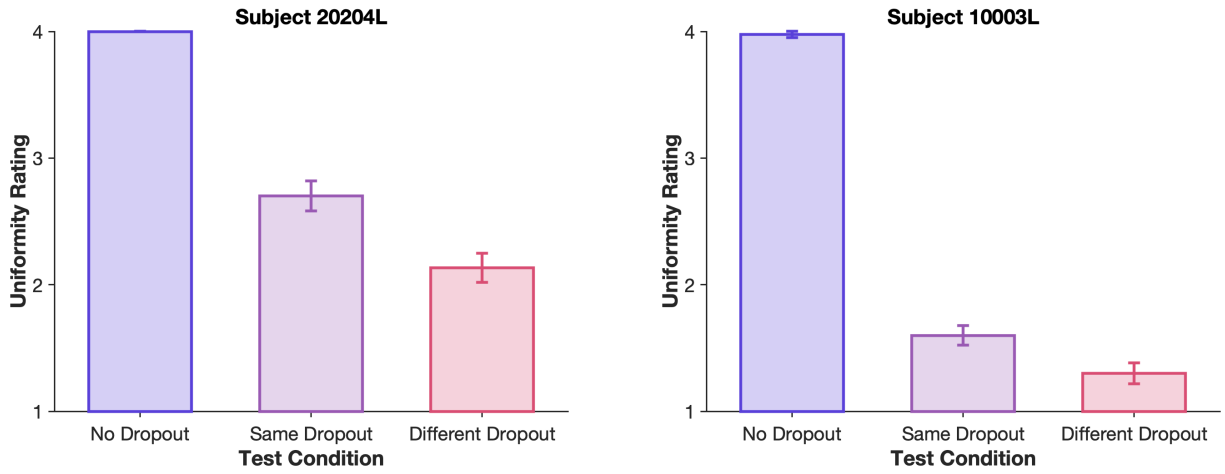

Figure 4.6: **Cone dropout adaptation experiment results.** The uniformity rating results are shown as bar charts for the adaptation experiment with 2 subjects. Each bar chart shows the average rating across all trials for the no dropout (blue), same dropout (purple), and different dropout (red) conditions. The left plot shows data from subject 20204L, who completed 90 trials, and the right plot shows data from subject 10003L, who completed 120 trials.

Results from this adaptation experiment are shown as bar charts in Figure 4.6. As expected, both subjects tended to rate the control no-dropout condition at a 4 in uniformity. Interestingly, there is a modest but reliable difference in ratings between the same-dropout (purple) and different-dropout (red) conditions for both subjects. For subject 20204L, this corresponded to an average rating of 2.7 across all trials for the same-dropout condition and 2.1 across all trials for the different-dropout condition. For subject 10003L these average ratings were 1.6 and 1.3 respectively. Despite the inter-subject differences in absolute rating magnitude, both subjects showed a tendency to rate the same-dropout condition higher in uniformity than the different-dropout condition. This suggests that an adaptation-like process indeed occurs during the initial 5-7 second stimulus presentation where the stimulus

image begins to appear more uniform. Moreover, this adaptation is specific to the spatial pattern of dropout, such that subjects preferentially rate uniformity higher when viewing stimuli with the same dropout map that they had previously adapted to. These results leave

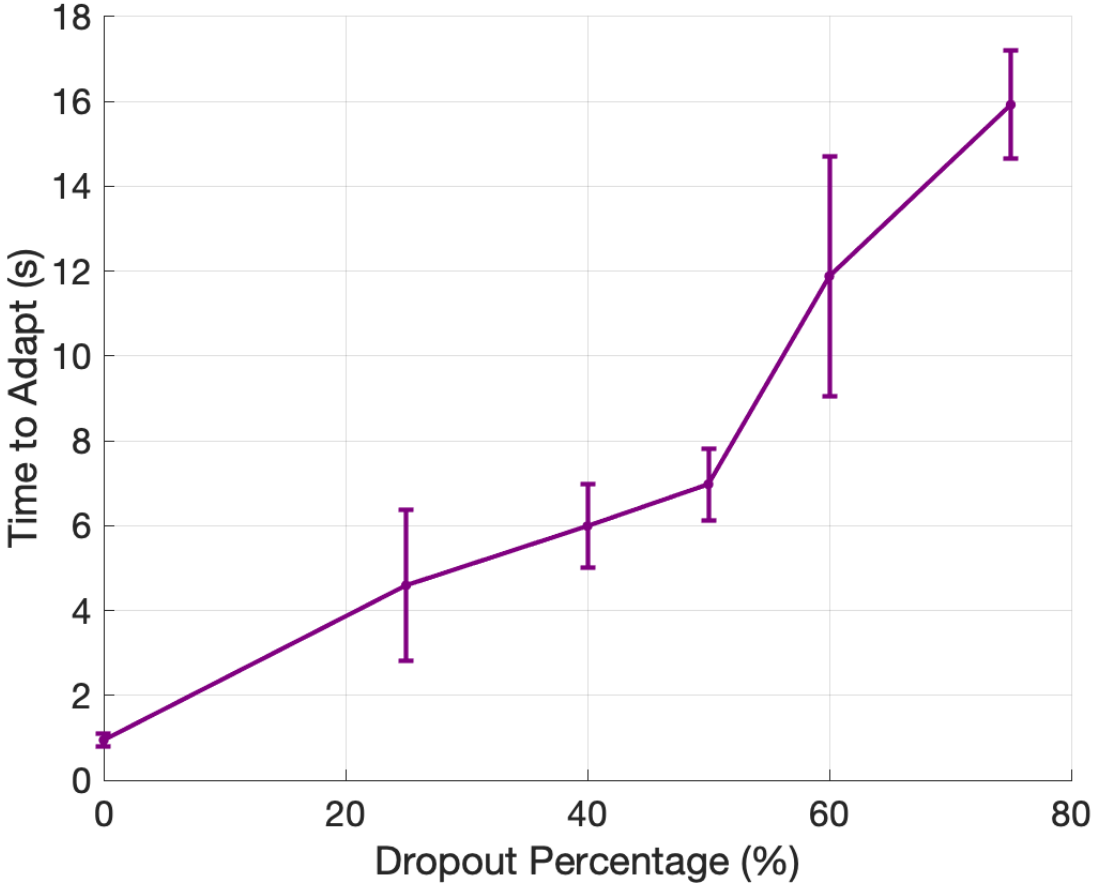

Figure 4.7: **Adaptation timecourse experiment results.** The time taken to adapt to a cone dropout pattern is plotted versus the dropout percentage. Each data point shows the average and standard error across 5 trials. Dropout patterns at 85% and 90% were presented to subjects, but are not plotted as the subjects did not indicate that they appeared uniform within the allotted 20 seconds.

opportunities for future exploration of the phenomenon. First, there is a clear difference in the absolute magnitude of the uniformity ratings between subjects for the dropout conditions. This difference could reflect either true differences in the subjects' perceptual experience, or it could be the result of differences in the internal criteria that subjects used to make their uniformity judgments. A further experiment could employ the use of a uniformity reference for each rating, in order to better standardize subject ratings and eliminate this confound.

Another opportunity for future study arises from the feature that the same-dropout condition was not rated as uniform as the no-dropout condition by either subject. This indicates that while the uniformity improved relative to another dropout condition, there remains a gap between the adapted dropout stimulus and an undegraded stimulus. This may reflect either a fundamental limit to the adaptation process, or that the parameters of the experiment did not allow for adaptation to take place to its fullest extent.

In order to determine the temporal requirements for full adaptation, we conducted a pilot experiment with one subject measuring the timecourse of adaptation as a function of dropout percentage. In this experiment, a randomized dropout map was applied to the retina while the subject viewed an image stimulus for up to 20 seconds. The stimuli were drawn from a set of 13 images, each consisting of a simple, 2-dimensional black and white object on a background set to 50% intensity. The subject was instructed to press a button when the image stimulus appeared to become fully uniform. In the experiment, 8 dropout percentages were tested ranging from 0% to 90%, and each percentage was shown for 5 trials in order to yield an average timecourse measurement for each condition.

The results of the timecourse experiment are shown in Figure 4.7. There is a clear increase in the time required to reach adaptation as the dropout percentage increases. Even at 75% dropout, the subject tended to indicate that the stimulus had become uniform after approximately 16 seconds. Although trials were shown above 80% dropout, the subject did not see the stimulus as uniform within the allotted 20 seconds, and thus these trials did not produce data points. While the subject's internal criteria for what appeared uniform in this experiment was subjective, this data establishes a measure of the relative increase in adaptation time with dropout, which can serve as a benchmark for future experiment designs. These preliminary experiments form the foundation for further exploration of this adaptation phenomenon.

4.6 Acknowledgments

This chapter was adapted from a manuscript that has been provisionally accepted at eLife, with co-authors James Fong, Ren Ng, and Austin Roorda. The authors thank Pavan Tiruveedhula for technical system support. This research was supported by funding from Air Force Office of Scientific Research grant FA9550-21-1-0230, National Institutes of Health grant R01EY023591 and the Minnie and Roseanna Turner Fund for Impaired Vision Research.

Chapter 5

Conclusion

In this dissertation, we outline a number of the physiological constraints which shape human color and spatial vision. We then describe a progression in retinal imaging and stimulation technology, culminating in our prototype system that enables unprecedented control over visual input at the retinal interface. Using this system, we characterize color perception of wavelengths beyond the visible range by eliciting 2-photon absorption of infrared light in cone cells. We show human subjects the color "olo" by targeting only M cones with laser stimulation. We programmatically modify the effective sampling density of the retina and measure the impact on visual acuity. In summary, we have utilized cone-level visual stimulation to decouple the retinal input from its spectral, chromatic, and spatial constraints and characterized perception outside of those bounds.

The three studies described here represent a fraction of what is possible with the Oz system, and many directions remain open for exploration. Future work could follow up on the final results described in Chapter 4 and probe the potential for long-term adaptation to cone dropout. Entirely different directions are also possible; for instance, this same system can be used to stimulate the retina as if an additional cone type has been added and determine whether the visual system can utilize it for expanded color vision [97]. From a technical standpoint, iterations on this prototype system face opportunities for improvement both in hardware and software. Future systems could replace visible-wavelength channels with a short-pulsed infrared light source in order to perform 2-photon Oz stimulation. Such a system would leverage the nonlinear power dependence of the 2-photon effect as described in Chapter 2 in order to mitigate the effects of light leak to non-target cones. In addition to this potential hardware upgrade, future versions of Wizard could add even further to the functionality of the Oz system and implement cone-by-cone rendering more generally. This could include the capability for presenting stimuli which move with a gain relative to eye motion [134], rendering of arbitrarily complex retinal modifications, and integration of Oz stimuli with a conventional RGB display. Ultimately, the work presented here marks a step toward complete control over the input to the visual system, with much progress still to come.

Bibliography

[1] H. Wässle. "Parallel processing in the mammalian retina". In: *Nature Reviews Neuroscience* 5.10 (2004), pp. 747–757.

[2] C. A. Curcio et al. "Human photoreceptor topography". eng. In: *The Journal of Comparative Neurology* 292.4 (Feb. 1990), pp. 497–523. ISSN: 0021-9967. DOI: 10.1002/cne.902920402.

[3] J. B. Jonas et al. "Histomorphometry of the human optic nerve." In: *Investigative Ophthalmology Visual Science* 31.4 (Apr. 1990), pp. 736–744. ISSN: 1552-5783.

[4] D. J. Felleman and D. C. Van Essen. "Distributed hierarchical processing in the primate cerebral cortex." In: *Cerebral cortex (New York, NY: 1991)* 1.1 (1991), pp. 1–47.

[5] J. J. DiCarlo, D. Zoccolan, and N. C. Rust. "How does the brain solve visual object recognition?" In: *Neuron* 73.3 (2012), pp. 415–434.

[6] A. J. Zele and D. Cao. "Vision under mesopic and scotopic illumination". English. In: *Frontiers in Psychology* 5 (Jan. 2015). Publisher: Frontiers. ISSN: 1664-1078. DOI: 10.3389/fpsyg.2014.01594.

[7] K.-W. Yau and R. C. Hardie. "Phototransduction motifs and variations". In: *Cell* 139.2 (2009), pp. 246–264.

[8] A. Stockman, L. T. Sharpe, and C. Fach. "The spectral sensitivity of the human short-wavelength sensitive cones derived from thresholds and color matches". eng. In: *Vision Research* 39.17 (Aug. 1999), pp. 2901–2927. ISSN: 0042-6989. DOI: 10.1016/s0042-6989(98)00225-9.

[9] A. Stockman and L. T. Sharpe. "The spectral sensitivities of the middle- and long-wavelength-sensitive cones derived from measurements in observers of known genotype". In: *Vision Research* 40.13 (June 2000), pp. 1711–1737. ISSN: 0042-6989. DOI: 10.1016/S0042-6989(00)00021-3.

[10] J. Nathans, D. Thomas, and D. S. Hogness. "Molecular Genetics of Human Color Vision: The Genes Encoding Blue, Green, and Red Pigments". In: *Science* 232.4747 (1986), pp. 193–202. DOI: 10.1126/science.2937147.

[11] J. C. Maxwell. "Experiments on Colour, as Perceived by the Eye, with Remarks on Colour-Blindness". In: *Transactions of the Royal Society of Edinburgh* 21.2 (1857), pp. 275–298.

[12] M. Fairchild. "Color Appearance Models". In: *Color Appearance Models*. Hoboken, New Jersey, USA: John Wiley & Sons, Aug. 2013, pp. 199–212. ISBN: 978-1-118-65312-8. DOI: 10.1002/9781118653128.ch10.

[13] F. W. Campbell and R. W. Gubisch. "Optical quality of the human eye". eng. In: *The Journal of Physiology* 186.3 (Oct. 1966), pp. 558–578. ISSN: 0022-3751. DOI: 10.1113/jphysiol.1966.sp008056.

[14] J. Francisco Castejón-Mochón et al. "Ocular wave-front aberration statistics in a normal young population". In: *Vision Research* 42.13 (June 2002), pp. 1611–1617. ISSN: 0042-6989. DOI: 10.1016/S0042-6989(02)00085-8.

[15] V. N. Mahajan. "Zernike Polynomials and Optical Aberrations". EN. In: *Applied Optics, Vol. 34, Issue 34, pp. 8060-8062* (Dec. 1995). Publisher: Optica Publishing Group. DOI: 10.1364/AO.34.008060.

[16] J. Liang and D. R. Williams. "Aberrations and retinal image quality of the normal human eye". EN. In: *JOSA A* 14.11 (Nov. 1997). Publisher: Optica Publishing Group, pp. 2873–2883. ISSN: 1520-8532. DOI: 10.1364/JOSAA.14.002873.

[17] L. N. Thibos et al. "The chromatic eye: a new reduced-eye model of ocular chromatic aberration in humans". EN. In: *Applied Optics* 31.19 (July 1992). Publisher: Optica Publishing Group, pp. 3594–3600. ISSN: 2155-3165. DOI: 10.1364/AO.31.003594.

[18] L. N. Thibos et al. "Theory and measurement of ocular chromatic aberration". In: *Vision Research* 30.1 (Jan. 1990), pp. 33–49. ISSN: 0042-6989. DOI: 10.1016/0042-6989(90)90126-6.

[19] L. N. Thibos. "Calculation of the influence of lateral chromatic aberration on image quality across the visual field". EN. In: *JOSA A* 4.8 (Aug. 1987). Publisher: Optica Publishing Group, pp. 1673–1680. ISSN: 1520-8532. DOI: 10.1364/JOSAA.4.001673.

[20] S. Winter et al. "Transverse chromatic aberration across the visual field of the human eye". In: *Journal of Vision* 16.14 (Nov. 2016), p. 9. ISSN: 1534-7362. DOI: 10.1167/16.14.9.

[21] C. Cherici et al. "Precision of sustained fixation in trained and untrained observers". In: *Journal of Vision* 12.6 (June 2012), p. 31. ISSN: 1534-7362. DOI: 10.1167/12.6.31.

[22] Y. Wang et al. "Human foveal cone photoreceptor topography and its dependence on eye length". In: *Elife* 8 (2019), e47148.

[23] M. Rucci et al. "Miniature eye movements enhance fine spatial detail". eng. In: *Nature* 447.7146 (June 2007), pp. 851–854. ISSN: 1476-4687. DOI: 10.1038/nature05866.

[24] J. Intoy and M. Rucci. "Finely tuned eye movements enhance visual acuity". eng. In: *Nature Communications* 11.1 (Feb. 2020), p. 795. ISSN: 2041-1723. DOI: 10.1038/s41467-020-14616-2.

[25] Z. Zhao et al. "Inferring visual space from ultra-fine extra-retinal knowledge of gaze position". eng. In: *Nature Communications* 14.1 (Jan. 2023), p. 269. ISSN: 2041-1723. DOI: 10.1038/s41467-023-35834-4.

[26] K. Ratnam et al. "Benefits of retinal image motion at the limits of spatial vision". In: *Journal of Vision* 17.1 (Jan. 2017), p. 30. ISSN: 1534-7362. DOI: 10.1167/17.1.30.

[27] P. K. Ahnelt. "The photoreceptor mosaic". en. In: *Eye* 12.3 (May 1998). Publisher: Nature Publishing Group, pp. 531–540. ISSN: 1476-5454. DOI: 10.1038/eye.1998.142.

[28] E. A. Rossi and A. Roorda. "The relationship between visual resolution and cone spacing in the human fovea". en. In: *Nature Neuroscience* 13.2 (Feb. 2010). Publisher: Nature Publishing Group, pp. 156–157. ISSN: 1546-1726. DOI: 10.1038/nn.2465.

[29] A. Roorda et al. "Adaptive optics scanning laser ophthalmoscopy". EN. In: *Optics Express* 10.9 (May 2002). Publisher: Optica Publishing Group, pp. 405–412. ISSN: 1094-4087. DOI: 10.1364/OE.10.000405.

[30] J. Liang, D. R. Williams, and D. T. Miller. "Supernormal vision and high-resolution retinal imaging through adaptive optics". eng. In: *Journal of the Optical Society of America. A, Optics, Image Science, and Vision* 14.11 (Nov. 1997), pp. 2884–2892. ISSN: 1084-7529. DOI: 10.1364/josaa.14.002884.

[31] A. Guirao et al. "Calculated impact of higher-order monochromatic aberrations on retinal image quality in a population of human eyes". EN. In: *JOSA A* 19.1 (Jan. 2002). Publisher: Optica Publishing Group, pp. 1–9. ISSN: 1520-8532. DOI: 10.1364/JOSAA.19.000001.

[32] H. Hofer, B. Singer, and D. R. Williams. "Different sensations from cones with the same photopigment". In: *J. Vis.* 5.5 (May 2005), pp. 5–5. ISSN: 1534-7362. DOI: 10.1167/5.5.5.

[33] C. M. Cicerone and J. L. Nerger. "The relative numbers of long-wavelength-sensitive to middle-wavelength-sensitive cones in the human fovea centralis". In: *Vision Research* 29.1 (1989), pp. 115–128. ISSN: 0042-6989. DOI: https://doi.org/10.1016/0042-6989(89)90178-8.

[34] S. B. Stevenson and A. Roorda. "Correcting for miniature eye movements in high resolution scanning laser ophthalmoscopy". In: *Ophthalmic Technologies XV*. Vol. 5688. Society of Photo-Optical Instrumentation Engineers (SPIE) Conference Series. In. Apr. SPIE, 2005, pp. 145–151. DOI: 10.1117/12.591190.

[35] D. W. Arathorn et al. "Retinally stabilized cone-targeted stimulus delivery". eng. In: *Optics Express* 15.21 (Oct. 2007), pp. 13731–13744. ISSN: 1094-4087. DOI: 10.1364/oe.15.013731.

[36] Q. Yang et al. "Design of an integrated hardware interface for AOSLO image capture and cone-targeted stimulus delivery". In: *Optics Express* 18.17 (Aug. 2010), pp. 17841–17858. ISSN: 1094-4087. DOI: 10.1364/OE.18.017841.

[37] W. M. Harmening et al. "Mapping the perceptual grain of the human retina". eng. In: *The Journal of Neuroscience: The Official Journal of the Society for Neuroscience* 34.16 (Apr. 2014), pp. 5667–5677. ISSN: 1529-2401. DOI: 10.1523/JNEUROSCI.5191-13.2014.

[38] A. Roorda and D. R. Williams. "The arrangement of the three cone classes in the living human eye". en. In: *Nature* 397.6719 (Feb. 1999). Publisher: Nature Publishing Group, pp. 520–522. ISSN: 1476-4687. DOI: 10.1038/17383.

[39] F. Zhang et al. "Cone photoreceptor classification in the living human eye from photostimulation-induced phase dynamics". eng. In: *Proceedings of the National Academy of Sciences of the United States of America* 116.16 (Apr. 2019), pp. 7951–7956. ISSN: 1091-6490. DOI: 10.1073/pnas.1816360116.

[40] V. P. Pandiyan et al. "High-speed adaptive optics line-scan OCT for cellular-resolution optoretinography". EN. In: *Biomedical Optics Express* 11.9 (Sept. 2020). Publisher: Optica Publishing Group, pp. 5274–5296. ISSN: 2156-7085. DOI: 10.1364/BOE.399034.

[41] V. P. Pandiyan et al. "Reflective mirror-based line-scan adaptive optics OCT for imaging retinal structure and function". eng. In: *Biomedical Optics Express* 12.9 (Sept. 2021), pp. 5865–5880. ISSN: 2156-7085. DOI: 10.1364/BOE.436337.

[42] V. P. Pandiyan et al. "Characterizing cone spectral classification by optoretinography". EN. In: *Biomedical Optics Express* 13.12 (Dec. 2022). Publisher: Optica Publishing Group, pp. 6574–6594. ISSN: 2156-7085. DOI: 10.1364/BOE.473608.

[43] R. Sabesan et al. "The elementary representation of spatial and color vision in the human retina". In: *Science Advances* 2.9 (Sept. 2016), e1600797. ISSN: 2375-2548. DOI: 10.1126/sciadv.1600797.

[44] B. P. Schmidt et al. "Sensations from a single M-cone depend on the activity of surrounding S-cones". In: *Scientific Reports* 8 (June 2018), p. 8561. ISSN: 2045-2322. DOI: 10.1038/s41598-018-26754-1.

[45] B. P. Schmidt et al. "The spectral identity of foveal cones is preserved in hue perception". In: *Journal of Vision* 18.11 (Oct. 2018), p. 19. ISSN: 1534-7362. DOI: 10.1167/18.11.19.

[46] B. P. Schmidt et al. "Spatial summation of individual cones in human color vision". en. In: *PLOS ONE* 14.7 (July 2019). Publisher: Public Library of Science, e0211397. ISSN: 1932-6203. DOI: 10.1371/journal.pone.0211397.

[47] J. Shenoy et al. "R-SLAM: Optimizing Eye Tracking from Rolling Shutter Video of the Retina". en. In: *2021 IEEE/CVF International Conference on Computer Vision (ICCV)*. Montreal, QC, Canada: IEEE, Oct. 2021, pp. 4832–4841. ISBN: 978-1-66542-812-5. DOI: 10.1109/ICCV48922.2021.00481.

[48] J. Fong et al. "Novel color via stimulation of individual photoreceptors at population scale". In: *Science Advances* 11.16 (2025), eadu1052. DOI: 10.1126/sciadv.adu1052.

[49] G. Palczewska et al. "Human infrared vision is triggered by two-photon chromophore isomerization". In: *Proceedings of the National Academy of Sciences* 111.50 (2014), E5445–E5454.

[50] D. R. Griffin, R. Hubbard, and G. Wald. "The Sensitivity of the Human Eye to Infra-Red Radiation". In: *J. Opt. Soc. Am.* 37.7 (1947), pp. 546–554.

[51] D. H. Sliney et al. "Visual sensitivity of the eye to infrared laser radiation". In: *J. Opt. Soc. Am.* 66.4 (1976), pp. 339–341.

[52] V. G. Dmitriev et al. "Nonlinear perception of infrared radiation in the 800–1355 nm range with human eye". In: *Soviet Journal of Quantum Electronics* 9.4 (1979), p. 475.

[53] P. L. Walraven and H. J. Leebeek. "Foveal Sensitivity of the Human Eye in the Near Infrared". In: *J. Opt. Soc. Am.* 53.6 (1963), pp. 765–766.

[54] L. H. Vasilenko, V. P. Chebotaev, and Y. V. Troitskii. "Visual observation of infrared laser emission". In: *J. Exptl. Theoret. Phys. (U.S.S.R.)* 48.3 (1965), pp. 777–994.

[55] T. Theodossiou et al. "Visual observation of infrared laser speckle patterns at half their fundamental wavelength". In: *Lasers in Medical Science* 16 (2001), pp. 34–39.

[56] Q. Zaidi and J. Pokorny. "Appearance of pulsed infrared light: second harmonic generation in the eye". In: *Appl. Opt.* 27.6 (1988), pp. 1064–1068.

[57] W. Denk, J. H. Strickler, and W. W. Webb. "Two-photon laser scanning fluorescence microscopy". In: *Science* 248.4951 (1990), pp. 73–76.

[58] P. Artal et al. "Visual acuity in two-photon infrared vision". In: *Optica* 4.12 (2017), pp. 1488–1491.

[59] O. Kaczkoś et al. "Methods of determining the contrast sensitivity function for two-photon vision". In: *22nd Polish-Slovak-Czech Optical Conference on Wave and Quantum Aspects of Contemporary Optics*. Vol. 12502. International Society for Optics and Photonics. SPIE, 2022, p. 1250215. DOI: 10.1117/12.2664174.

[60] M. Marzejon et al. "Effects of laser pulse duration in two-photon vision threshold measurements". In: *Ophthalmic Technologies XXXI*. Vol. 11623. International Society for Optics and Photonics. SPIE, 2021, 116231N.

[61] G. Łabuz et al. "Clinical application of infrared-light microperimetry in the assessment of scotopic-eye sensitivity". In: *Translational Vision Science & Technology* 9.8 (2020), pp. 7–7. ISSN: 2164-2591.

[62] G. Łabuz et al. "The loss of infrared light sensitivity of photoreceptor cells measured with two-photon excitation as an indicator of diabetic retinopathy: a pilot study". In: *Retina* 41.6 (2021), pp. 1302–1308.

[63] A. Wei et al. "Two-photon microperimetry: a media opacity-independent retinal function assay". In: *Transl Vis Sci Technol.* 10.2 (2021), p. 11.

[64] U. Mehta et al. "Seeing invisible light: 2-photon microperimetry to measure visual function". In: *Am J Ophthalmol Case Rep.* 28 (2022), p. 101724.

[65] D. Ruminski et al. "Two-photon microperimetry: sensitivity of human photoreceptors to infrared light". In: *Biomedical Optics Express* 10.9 (2019), pp. 4551–4567.

[66] M. J. Marzejon et al. "Two-photon microperimetry with picosecond pulses". In: *Biomedical Optics Express* 12.1 (2021), pp. 462–479.

[67] W. M. Harmening et al. "Measurement and correction of transverse chromatic offsets for multi-wavelength retinal microscopy in the living eye". eng. In: *Biomedical Optics Express* 3.9 (Sept. 2012), pp. 2066–2077. ISSN: 2156-7085. DOI: 10.1364/BOE.3.002066.

[68] H. K. Doyle et al. "Boosting 2-photon vision with adaptive optics". In: *Journal of Vision* 23.12 (2023), pp. 4–4.

[69] ANSI. *American National Standard for Safe Use of Lasers*. Laser Institute of America, 2014.

[70] S. Mozaffari et al. "Wide-vergence, multi-spectral adaptive optics scanning laser ophthalmoscope with diffraction-limited illumination and collection". In: *Biomedical Optics Express* 11.3 (2020). Publisher: Optica Publishing Group, pp. 1617–1632.

[71] N. Domdei et al. "Ultra-high contrast retinal display system for single photoreceptor psychophysics". In: *Biomedical Optics Express* 9.1 (2018), pp. 157–172.

[72] D. H. Brainard. "The psychophysics toolbox". In: *Spatial Vision* 10.4 (1997). Place: Leiden, The Netherlands Publisher: Brill, pp. 433–436.

[73] D. G. Pelli. "The videotoolbox software for visual psychophysics: transforming numbers into movies". English (US). In: *Seeing and Perceiving* 10.4 (1997). Publisher: Brill, pp. 437–442. ISSN: 2213-4794.

[74] M. Kleiner et al. "What's new in psychtoolbox-3". English (US). In: *Perception* 36.14 (2007). Publisher: Pion Ltd., pp. 1–16. ISSN: 0301-0066.

[75] H. Cheng et al. "A population study on changes in wave aberrations with accommodation". In: *Journal of Vision* 4.4 (2004), pp. 3–3. ISSN: 1534-7362.

[76] NKT Photonics. *ORIGAMI LP – ultra-low noise femtosecond lasers*. 2022.

[77] Menlo Systems. *Orange Femtosecond Ytterbium Laser*. 2023.

[78] ThorLabs, Inc. *FSL1030X2 - Ytterbium Femtosecond Fiber Laser*. 2023.

[79] X. Jiang et al. "Measuring and compensating for ocular longitudinal chromatic aberration". In: *Optica* 6.8 (2019), pp. 981–990.

[80] J. C. Celentano, J. D. Burke, and B. R. Hammond Jr. "In vivo assessment of retinal carotenoids: macular pigment detection techniques and their impact on monitoring pigment status". In: *The Journal of Nutrition* 132.3 (2002), 535S–539S. ISSN: 0022-3166.

[81] M. A. Webster et al. "Colour appearance and compensation in the near periphery". In: *Proceedings of the Royal Society B: Biological Sciences* 277.1689 (2010), pp. 1817–1825.

[82] R. A. Bone, J. T. Landrum, and A. Cains. "Optical density spectra of the macular pigment in vivo and in vitro". In: *Vision Research* 32.1 (1992), pp. 105–110. ISSN: 0042-6989.

[83] J. C. Maxwell. "The theory of the primary colours". In: *British Journal of Photography* 9 (1861).

[84] G. S. Brindley. "The effects on colour vision of adaptation to very bright lights". In: *J. Physiol.* 122.2 (Nov. 1953), pp. 332–350. ISSN: 0022-3751. DOI: 10.1113/jphysiol.1953.sp005003.

[85] R. S. Harwerth and H. G. Sperling. "Prolonged Color Blindness Induced by Intense Spectral Lights in Rhesus Monkeys". In: *Science* 174.4008 (Oct. 1971). Publisher: American Association for the Advancement of Science, pp. 520–523. DOI: 10.1126/science.174.4008.520.

[86] P. Churchland. "Chimerical colors: some phenomenological predictions from cognitive neuroscience". In: *Philosophical Psychology* 18.5 (Oct. 2005), pp. 527–560. ISSN: 0951-5089. DOI: 10.1080/09515080500264115.

[87] O. Estévez and H. Spekreijse. "The "silent substitution" method in visual research". In: *Vision Res.* 22.6 (Jan. 1982), pp. 685–686. ISSN: 0042-6989. DOI: 10.1016/0042-6989(82)90104-3.

[88] R. L. De Valois et al. "Hue Scaling of Isoluminant and Cone-specific Lights". In: *Vision Res.* 37.7 (Apr. 1997), pp. 885–897. ISSN: 0042-6989. DOI: 10.1016/S0042-6989(96)00234-9.

[89] W. M. Harmening and L. C. Sincich. "Adaptive Optics for Photoreceptor-Targeted Psychophysics". In: *High Resolution Imaging in Microscopy and Ophthalmology: New Frontiers in Biomedical Optics*. Cham: Springer International Publishing, 2019, pp. 359–375. ISBN: 978-3-030-16638-0. DOI: 10.1007/978-3-030-16638-0_17.

[90] J. Koenderink et al. "Hues of Color Afterimages". In: *i-Perception* 11.1 (Jan. 2020), p. 2041669520903553. ISSN: 2041-6695. DOI: 10.1177/2041669520903553.

[91] J. E. Vanston et al. "It's not easy seeing green: The veridical perception of small spots". In: *J. Vis.* 23.5 (2023), pp. 2–2.

[92] J. Freeman et al. "Mapping nonlinear receptive field structure in primate retina at single cone resolution". In: *eLife* 4 (Oct. 2015). Ed. by M. Carandini. Publisher: eLife Sciences Publications, Ltd, e05241. ISSN: 2050-084X. DOI: 10.7554/eLife.05241.

[93] J. B. Demb et al. "Functional Circuitry of the Retinal Ganglion Cell's Nonlinear Receptive Field". In: *J. Neurosci.* 19.22 (Nov. 1999), p. 9756. DOI: 10.1523/JNEUROSCI.19-22-09756.1999.

[94] D. R. Coates et al. "The Rayleigh limit of the parvocellular pathway". In: *Invest. Ophthalmol. Vis. Sci.* 60.9 (July 2019), pp. 1312–1312. ISSN: 1552-5783.

[95] A. M. Geller, P. A. Sieving, and D. G. Green. "Effect on grating identification of sampling with degenerate arrays". eng. In: *Journal of the Optical Society of America. A, Optics and Image Science* 9.3 (Mar. 1992), pp. 472–477. ISSN: 0740-3232. DOI: 10.1364/josaa.9.000472.

[96] K. Ratnam et al. "Relationship Between Foveal Cone Structure and Clinical Measures of Visual Function in Patients With Inherited Retinal Degenerations". In: *Investigative Ophthalmology & Visual Science* 54.8 (Aug. 2013), pp. 5836–5847. ISSN: 0146-0404. DOI: 10.1167/iovs.13-12557.

[97] K. Mancuso et al. "Gene therapy for red–green colour blindness in adult primates". In: *Nature* 461.7265 (Oct. 2009), pp. 784–787. ISSN: 1476-4687. DOI: 10.1038/nature08401.

[98] G. H. Jacobs. "Photopigments and the dimensionality of animal color vision". In: *Neurosci. Biobehav. Rev.* 86 (2018), pp. 108–130.

[99] D. A. Atchison and G. Smith. "Chromatic dispersions of the ocular media of human eyes". In: *J. Opt. Soc. Am. A* 22.1 (2005), pp. 29–37.

[100] A. E. Boehm et al. "Transverse chromatic offsets with pupil displacements in the human eye: sources of variability and methods for real-time correction". In: *Biomedical Optics Express* 10.4 (Apr. 2019), pp. 1691–1706. DOI: 10.1364/BOE.10.001691.

[101] K. G. Foote et al. "Relationship Between Foveal Cone Structure and Visual Acuity Measured With Adaptive Optics Scanning Laser Ophthalmoscopy in Retinal Degeneration". In: *Investigative Ophthalmology & Visual Science* 59.8 (July 2018), pp. 3385–3393. ISSN: 0146-0404. DOI: 10.1167/iovs.17-23708.

[102] M. Georgiou, K. Fujinami, and M. Michaelides. "Inherited retinal diseases: Therapeutics, clinical trials and end points—A review". In: *Clinical & Experimental Ophthalmology* 49.3 (2021), pp. 270–288.

[103] B. Jones et al. "Retinal Remodeling in Human Retinitis Pigmentosa". In: *Experimental eye research* 150 (Sept. 2016), pp. 149–165. ISSN: 0014-4835. DOI: 10.1016/j.exer.2016.03.018.

[104] J. Y. Lee et al. "Impact of Photoreceptor Loss on Retinal Circuitry". en. In: *Annual Review of Vision Science* 7.Volume 7, 2021 (Sept. 2021). Publisher: Annual Reviews, pp. 105–128. ISSN: 2374-4642, 2374-4650. DOI: 10.1146/annurev-vision-100119-124713.

[105] W. Seiple et al. "The effects of random element loss on letter identification: implications for visual acuity loss in patients with retinitis pigmentosa". eng. In: *Vision Research* 35.14 (July 1995), pp. 2057–2066. ISSN: 0042-6989. DOI: 10.1016/0042-6989(94)00289-x.

[106] K. R. Alexander et al. "Effect of spatial sampling on grating resolution and letter identification". eng. In: *Journal of the Optical Society of America. A, Optics, Image Science, and Vision* 12.9 (Sept. 1995), pp. 1825–1833. ISSN: 1084-7529. DOI: 10.1364/josaa.12.001825.

[107] A. K. Krishnan et al. "Impact of simulated micro-scotomas on reading performance in central and peripheral retina". eng. In: *Experimental Eye Research* 183 (June 2019), pp. 9–19. ISSN: 1096-0007. DOI: 10.1016/j.exer.2018.06.027.

[108] H. D. Crane and D. H. Kelly. "Accurate simulation of visual scotomas in normal subjects". EN. In: *Applied Optics* 22.12 (June 1983). Publisher: Optica Publishing Group, pp. 1802–1806. ISSN: 2155-3165. DOI: 10.1364/AO.22.001802.

[109] E. M. Fine and G. S. Rubin. "Effects of Cataract and Scotoma on Visual Acuity: A Simulation Study". en-US. In: *Optometry and Vision Science* 76.7 (July 1999), p. 468. ISSN: 1538-9235.

[110] M. Kwon et al. "Contour Enhancement Benefits Older Adults with Simulated Central Field Loss". en-US. In: *Optometry and Vision Science* 89.9 (Sept. 2012), p. 1374. ISSN: 1538-9235. DOI: 10.1097/OPX.0b013e3182678e52.

[111] L. McIlreavy, J. Fiser, and P. J. Bex. "Impact of Simulated Central Scotomas on Visual Search in Natural Scenes". en-US. In: *Optometry and Vision Science* 89.9 (Sept. 2012), p. 1385. ISSN: 1538-9235. DOI: 10.1097/OPX.0b013e318267a914.

[112] P. R. Jones et al. "Seeing other perspectives: evaluating the use of virtual and augmented reality to simulate visual impairments (OpenVisSim)". en. In: *npj Digital Medicine* 3.1 (Mar. 2020). Publisher: Nature Publishing Group, p. 32. ISSN: 2398-6352. DOI: 10.1038/s41746-020-0242-6.

[113] H. Chow-Wing-Bom, T. M. Dekker, and P. R. Jones. "The worse eye revisited: Evaluating the impact of asymmetric peripheral vision loss on everyday function". In: *Vision Research* 169 (Apr. 2020), pp. 49–57. ISSN: 0042-6989. DOI: 10.1016/j.visres.2019.10.012.

[114] A. Sipatchin, M. G. García, and S. Wahl. "Target Maintenance in Gaming via Saliency Augmentation: An Early-Stage Scotoma Simulation Study Using Virtual Reality (VR)". en. In: *Applied Sciences* 11.15 (Aug. 2021). ISSN: 2076-3417. DOI: 10.3390/app11157164.

[115] M. Barbieri et al. "Assessing REALTER simulator: analysis of ocular movements in simulated low-vision conditions with extended reality technology". English. In: *Frontiers in Bioengineering and Biotechnology* 12 (Apr. 2024). Publisher: Frontiers. ISSN: 2296-4185. DOI: 10.3389/fbioe.2024.1285107.

[116] K. Holmqvist and P. Blignaut. "Small eye movements cannot be reliably measured by video-based P-CR eye-trackers". eng. In: *Behavior Research Methods* 52.5 (Oct. 2020), pp. 2098–2121. ISSN: 1554-3528. DOI: 10.3758/s13428-020-01363-x.

[117] A. G. Anderson et al. "High-acuity vision from retinal image motion". In: *Journal of Vision* 20.7 (July 2020), p. 34. ISSN: 1534-7362. DOI: 10.1167/jov.20.7.34.

[118] A. B. Watson and D. G. Pelli. "Quest: A Bayesian adaptive psychometric method". en. In: *Perception & Psychophysics* 33.2 (Mar. 1983), pp. 113–120. ISSN: 1532-5962. DOI: 10.3758/BF03202828.

[119] D. V. Walsh and L. Liu. "Adaptation to a simulated central scotoma during visual search training". In: *Vision Research* 96 (Mar. 2014), pp. 75–86. ISSN: 0042-6989. DOI: 10.1016/j.visres.2014.01.005.

[120] H. Yu and M. Kwon. "Altered Eye Movements During Reading With Simulated Central and Peripheral Visual Field Defects". In: *Investigative Ophthalmology & Visual Science* 64.13 (Oct. 2023), p. 21. ISSN: 0146-0404. DOI: 10.1167/iovs.64.13.21.

[121] J. Reinhard et al. "Quantifying fixation in patients with Stargardt disease". In: *Vision Research* 47.15 (July 2007), pp. 2076–2085. ISSN: 0042-6989. DOI: 10.1016/j.visres.2007.04.012.

[122] G. Kumar and S. T. L. Chung. "Characteristics of Fixational Eye Movements in People With Macular Disease". In: *Investigative Ophthalmology & Visual Science* 55.8 (Aug. 2014), pp. 5125–5133. ISSN: 1552-5783. DOI: 10.1167/iovs.14-14608.

[123] E. Bensinger et al. "Loss of Foveal Cone Structure Precedes Loss of Visual Acuity in Patients With Rod-Cone Degeneration". In: *Investigative Ophthalmology & Visual Science* 60.8 (July 2019), pp. 3187–3196. ISSN: 0146-0404. DOI: 10.1167/iovs.18-26245.

[124] K. S. Bruce et al. "Normal Perceptual Sensitivity Arising From Weakly Reflective Cone Photoreceptors". eng. In: *Investigative Ophthalmology & Visual Science* 56.8 (July 2015), pp. 4431–4438. ISSN: 1552-5783. DOI: 10.1167/iovs.15-16547.

[125] J. H. Tu et al. "Dysflective cones: Visual function and cone reflectivity in long-term follow-up of acute bilateral foveolitis". In: *American Journal of Ophthalmology Case Reports* 7 (Apr. 2017), pp. 14–19. ISSN: 2451-9936. DOI: 10.1016/j.ajoc.2017.04.001.

[126] D. Palanker and G. Goetz. "Restoring Sight with Retinal Prostheses". In: *Physics today* 71.7 (July 2018), pp. 26–32. ISSN: 0031-9228. DOI: 10.1063/PT.3.3970.

[127] F. G. Holz et al. "Subretinal Photovoltaic Implant to Restore Vision in Geographic Atrophy Due to AMD". In: *New England Journal of Medicine* 0.0 (2025). ISSN: 0028-4793. DOI: 10.1056/NEJMoa2501396.

[128] K. Turano and X. Wang. "Motion thresholds in retinitis pigmentosa". eng. In: *Investigative Ophthalmology & Visual Science* 33.8 (July 1992), pp. 2411–2422. ISSN: 0146-0404.

[129] K. R. Alexander et al. "Discrimination of spatial displacements by patients with retinitis pigmentosa". In: *Vision Research* 38.8 (Apr. 1998), pp. 1171–1181. ISSN: 0042-6989. DOI: 10.1016/S0042-6989(97)00235-6.

[130] A. M. Geller and P. A. Sieving. "Assessment of foveal cone photoreceptors in Stargardt's macular dystrophy using a small dot detection task". eng. In: *Vision Research* 33.11 (July 1993), pp. 1509–1524. ISSN: 0042-6989. DOI: 10.1016/0042-6989(93)90144-l.

[131] W. Makous et al. "Retinal Microscotomas Revealed with Adaptive-Optics Microflashes". In: *Investigative Ophthalmology & Visual Science* 47.9 (Sept. 2006), pp. 4160–4167. ISSN: 1552-5783. DOI: 10.1167/iovs.05-1195.

[132] K. R. Alexander, D. J. Derlacki, and G. A. Fishman. "Contrast thresholds for letter identification in retinitis pigmentosa". eng. In: *Investigative Ophthalmology & Visual Science* 33.6 (May 1992), pp. 1846–1852. ISSN: 0146-0404.

[133] C. R. Lindberg et al. "Contrast sensitivity in retinitis pigmentosa." In: *The British Journal of Ophthalmology* 65.12 (Dec. 1981), pp. 855–858. ISSN: 0007-1161.

[134] J. C. D'Angelo et al. "A paradoxical misperception of relative motion". In: *Proceedings of the National Academy of Sciences* 121.48 (Nov. 2024). Publisher: Proceedings of the National Academy of Sciences, e2410755121. DOI: 10.1073/pnas.2410755121.